

**Schedule for Presentation Meeting of Master-Degree Thesis in 2019**  
**International Course of Maritime & Urban Engineering**

Date : July 31st (Wednesday) starting from 09:30

Venue : S1-312 Lecture Room

No.	Time	Name	Supervisor	Title of thesis	Chairman
1	09:30 – 09:55	Win Naing Htay	Toda	A CFD-based Comparison Study of Conventional Rudder and Rudder with Bulb-Fins System of KVLCC2 in Waves	Sanada
2	09:55 – 10:20	Aye Nyein Mon	Aoki	An Experimental Study on the Stability of Filter Units on Rubble Mound Breakwater	Sanada
3	10:20 – 10:45	SAMDANI H M Golam	Sanada	Experimental Study on a Strengthening Technique by Wing Walls for Flat Plate-Column Connections with Low-Strength Concrete	Sanada
4	10:50 – 11:15	Phyo Myat Kyaw	Osawa	Development of an Influence Coefficient Database for Evaluating Mixed-mode SIFs and Application to Inclined Surface Cracks in Semi-infinite Bodies	Iijima
5	11:15 – 11:40	HONG Yang	Kashiwagi	Numerical Calculation Method for Hydroelastic Response of a Ship with Forward Speed in Waves Using Orthogonal Mathematical Mode Functions	Iijima
Lunch Break					
6	13:00 – 13:25	MANIYAPPAN Sreenath	Umeda	Effectiveness and Mechanism of Broaching-To Prevention Using Global Optimal Control (CMA-ES)	Irie
7	13:25 – 13:50	WANG Yueyi	Irie	A numerical study on water environment prediction in Lake Kasumigaura using unstructured grid three-dimensional flow model	Irie
8	13:50 – 14:15	KALAMBAY Ilunga Panick	Doi	Safety Performance Analysis of Unsignalized mid-block Crosswalks: An Agent-based Approach for Pedestrian-vehicle Interactions	Irie
Break					
9	14:30 – 14:55	REN Xu	Toda	Full Scale resistance prediction of paint surface -Proposal of new approximate formula for friction with roughness	Suzuki
10	14:55 – 15:20	YAO Yujia	Suzuki	Study on Dolphin Swimming Performance by CFD	Suzuki
11	15:20 – 15:45	ABDUL HALIM Azhan Bin	Osawa	Study on Measurement Method of Under-Film Corrosion's Incubation Life Using Fe (II) Fluorescent Indicator	Suzuki
	16:00 –	at S1-323 Meeting for Evaluating Mater-thesis Presentations, and Steering Committee Meeting			

Meeting for Evaluation: From 16:00 at S1-323 Meeting Room  
Members are Steering committee members and the supervisors

# A CFD-Based Comparison Study of Conventional Rudder and Rudder with Bulb-Fins System of KVLCC2 in Waves

Win Naing Htay

Hull Form Design Sub-Area, Department of Naval Architecture and Ocean Engineering

**Key Words:** Energy-Saving Device, Rudder Bulb-Fins System (RBFS), CFD, Propulsion Performance, Head Waves

## 1. Introduction

Recently pressure with respect to greenhouse gas reduction on ship-designers and yards is increasing considerably due to environmental concerns. As a result, International Maritime Organization (IMO) published a new mandatory concept named as Energy Efficiency Design Index (EEDI), in order to improve energy efficiency and eliminate inefficient ships from the market. An industry driven by eco-friendliness, which signifies that developing core technologies to cut greenhouse gas emission of ships will be increasingly essential. Climbing oil prices also raise the necessity to develop Energy-Saving Devices (ESDs) which minimize the energy loss during sail or partially recover the lost energy. Rudder Bulb-Fins System (RBFS) is one of the ESDs to solve this problems. These RBFS can recover rotational flow behind the propeller.

The performance of RBFS in calm water by installing the fins with angle of attack on both sides and finding out the best angle of attack which gives the most efficient fin have been investigated both experimentally and by using Computational Fluid Dynamics (CFD) method<sup>1)</sup>. It must be emphasized that design is aimed at good performance not only for the model test or trial condition in calm seas but also for the service conditions with wind and waves. Therefore, the objective of this research is to investigate the performance of RBFS and to compare with conventional rudder in different head waves conditions.

## 2. Methodology

The prediction of self-propulsion factors and flow field parameters of KRISO Very Large Crude Carrier (KVLCC2) of length between perpendiculars (Lpp) 3.2m with Froude number of 0.142 and two degree of freedom (heave and pitch) conditions in regular head waves has been done by using CFDSHIP-IOWA<sup>2)</sup>. It is a general-purpose unsteady RANS or DES code coupling with motion solver. The  $k-\omega$  SST turbulence model was employed. A single phase level-set method has been used to model the free surface and two degree of freedom (DOF) motions are considered. The grids comprising of 15 blocks for RBFS and 11 blocks for conventional rudder have been generated using Gridgen. Thereafter SUGGAR library has been used for the overset of grids. The computational domain and boundary condition is shown in Fig. 1. A no slip boundary condition with  $u=0$  and ( $v$  and  $w$ ) are specified based on propeller angular velocity;  $2\pi r_{\text{hub}} n$  is imposed on the hub surface;  $r_{\text{hub}}$  is the radius at the grid point on the hub surface and  $n$  is the propeller revolution rate.  $u, v, w$  are the velocity component in  $x, y, z$  direction.  $x, y, z$  are longitudinal direction, starboard direction and vertical upward direction respectively. All variable are non-dimensionalized by ship speed  $U$ , ship Length  $L$ , density  $\rho$  and their combinations.

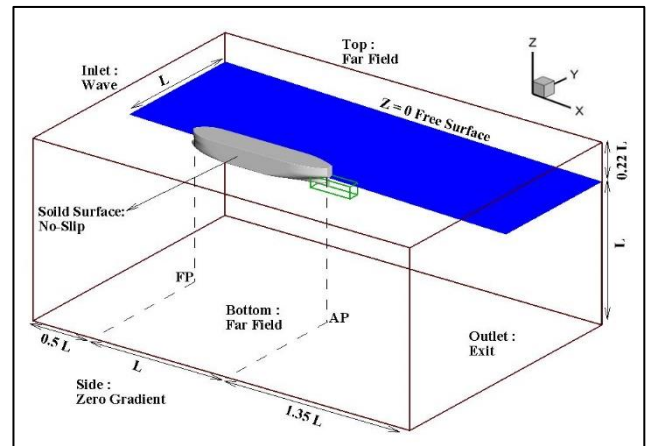


Fig. 1 Computational domain and boundary conditions.

## 3. Simulation Results

### 3.1 Ship motions

The time history comparison of heave and pitch motions between RBFS and conventional rudder in wave of  $\lambda/L = 1.1$  with amplitude of 3cm for one encounter period has been shown in Figure. 2 together with waves at bow and propeller plane. The time history of wave elevations at bow and propeller section are calculated by the equation of  $\zeta = A \cos(kx - \omega_e t)$ . The amplitude and phase of heave and pitch motion in RBFS are almost same with that in conventional rudder. However, the average values of ship motions in RBFS seems to be more negative (larger sinkage and bow down trim) as compared to conventional rudder.

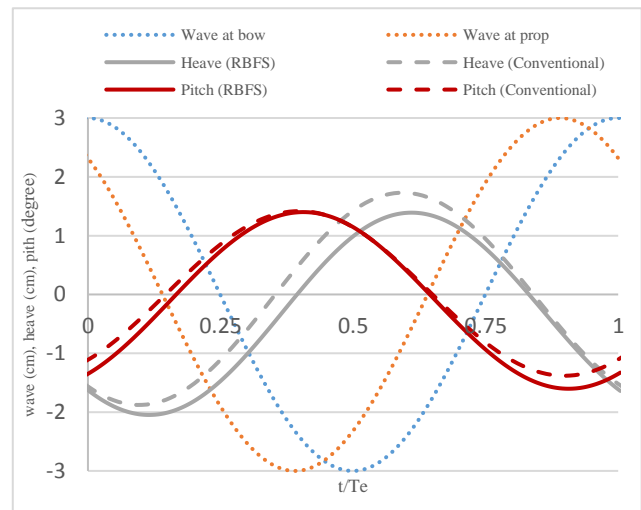


Fig. 2 Comparison of ship motion between RBFS and conventional rudder in  $\lambda/L = 1.1$  for one encounter period.

### 3.2 Flow field analysis

Figure 3 plots the axial velocity contour ( $u/U$ ) and cross flow vectors ( $v, w$ ) at  $x/L = 1$ , AP position across the rudder, bulb and fins, for  $\lambda/L = 1.1$  at  $t/Te=0$ , wave crest at bow. The hub vortex attaches on the portside surface of the rudder and a downward flow is caused on the starboard side surface in both rudders. As compared to conventional rudder, the hub vortex location is lowered due to rudder bulb and fins and hub vortex area is smaller in RBFS.

To understand the vortex structure, Q-Criterion is used. In figure 4, Q value of 500 is used for visualizing vortex for  $\lambda/L = 1.1$  at  $t/Te = 0$ . The region where the selected Q value is matched, iso-surface is created and colored with axial velocity contour ( $u/U$ ). The effect of rudder bulb and fins and the way of how they deform the hub vortex are obvious in that figure. The propeller tip vortex and hub vortex can be seen clearly and the hub vortex in port side of rudder is stronger than the starboard side's one in both rudders. This is because of the clockwise rotation of propeller. Additionally, the rudder fin tip vortex is occurred in the vortex visualization of RBFS.

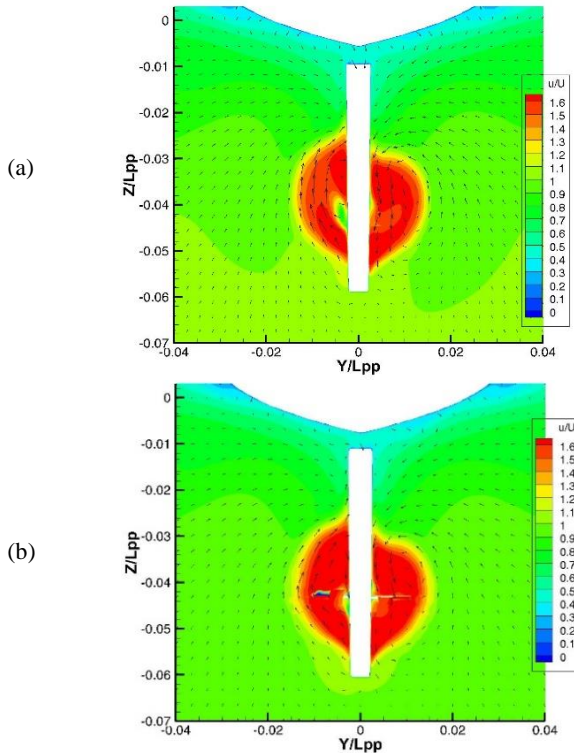


Fig. 3 Axial velocity section in one encounter period for  $\lambda/L = 1.1$  in  $x/L = 1$  at  $t/Te=0$  (a) conventional rudder (b) RBFS.

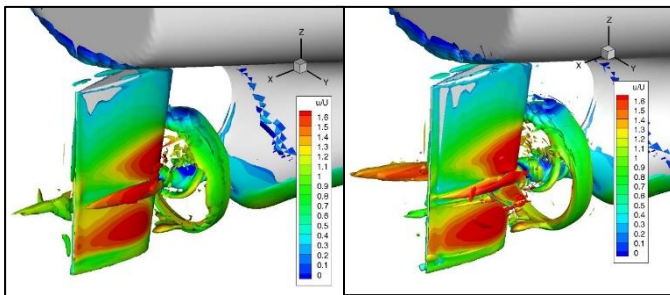


Fig. 4 Illustration of Q-criterion for  $Q=500$  colored by the axial velocity contours for  $\lambda/L = 1.1$  at  $t/Te = 0$  (Left: conventional rudder, Right: RBFS).

### 3.3 Self-propulsion

Table 1 shows the summary of mean values of thrust, wake fraction and hull efficiency between RBFS and conventional rudder to know the improvement by the RBFS. Rudder bulb and fins can reduce the resistance because the shape of bulb and fins makes the ship stern flow smooth and reduce the vorticity. However, the thrust is lower slightly in RBFS only in  $\lambda/L = 1.6$ , long wave conditions. In the result of effective wake, it is reduced a little in all wave conditions except in  $\lambda/L = 1.6$ , long wave condition. As KVLCC2 is tanker shape and the wake field is wide so that the effective wake factor is lower in all conditions. Regarding to that table, hull efficiency,  $\eta_H$  is improved by rudder bulb and fins in all wave conditions except long wave,  $\lambda/L = 1.6$ . From these comparison, RBFS does not have very bad effect in waves and some improvement in short and medium wave length.

Table 1 Summary of self-propulsion factors.

Waves ( $\lambda/L$ )	Rudder Types	Thrust (N)	1-t	1-w	$\eta_H$
0.6	Normal	4.9028	0.7993	0.4631	1.7257
	RBFS	4.9288	0.7920	0.4571	1.7326
1.1	Normal	4.8786	0.8174	0.4679	1.7467
	RBFS	4.9533	0.8190	0.4514	1.8145
1.6	Normal	4.9673	0.8031	0.4465	1.7988
	RBFS	4.9445	0.8076	0.4532	1.7820

### 4. Conclusions

There is no significant difference in ship motions (heave and pitch) of between RBFS and conventional rudder.

In flow field analysis, the strength of hub vortex decreases due to the rudder bulb. Its area and velocity around core is smaller in RBFS than in normal rudder. The interaction of fin and ship motion can be observed in waves.

As compared to the conventional rudder, the resistance decreases on RBFS in all wave conditions. On the other hand, thrust is improved by rudder fins. Increase of hull efficiency and decrease of open water efficiency are found in self-propulsion analysis. Generally, overall quasi-propulsive efficiency improves a little bit because of the rudder bulb and fins.

For the future work, it is necessary to validate the CFD results with experimental results. That's why experiment will be conducted using the KVLCC2 ship model with the same conditions as CFD case in towing tank of Osaka University.

### References

- 1) Truong, T. Q., Wu, P.-C., Aoyagi, K., Koike, K., Akiyama, Y. and Toda, Y. (2017) "The EFD and CFD Study of Rudder-Bulb-Fin System in Ship and Propeller Wake Field of KVLCC2 Tanker in Calm Water", 27<sup>th</sup> ISOPE conference, California, USA.
- 2) Paterson, G., Wilson, W. and Stern, F.: "General-purpose parallel Unsteady RANS Ship Hydrodynamics Code." CFDShip-IOWA, IIHR Report No.432, pp.2-21, 2003.

# An Experimental Study on the Stability of Filter Units on Rubble Mound Breakwater

Aye Nyein Mon

Coastal Engineering Laboratory, Department of Civil Engineering

**Key Words:** filter unit, FU damage, stability coefficient, Hudson formula

## 1. Introduction

Filter unit (FU) is a stone-filled net made of synthetic fiber. The FU was used first in rivers in order to prevent scouring of river banks. Any type of solid materials such as stones, pebbles, crushed concrete, etc. can be used as the filling material. The FU can be placed on rougher surfaces because of its flexibility compared with conventional materials<sup>1)</sup>. Therefore, the FU has recently been used also in coastal works.

When FUs are used in coastal engineering work, it has identified that the filling stone movement generated by wave action causes deformation and displacement of the FU. Further, violent collision of the filling stones with the synthetic fiber would damage the net. To overcome these problems, restraining filling material need to be done which can not only increase the hydraulic stability but also durability of filter net. Therefore, a rope restraining method was adopted<sup>1)</sup>. The FU, that is tied with a constraining rope from top to bottom, is referred to as the restricted type (S-type FU) and the conventional unit that is widely used for rivers is referred to as the normal type (N-type FU). In addition, there is a newly developed FU by a Japanese Company, which is called "Rock Unit (RU)" (see fig. 1).

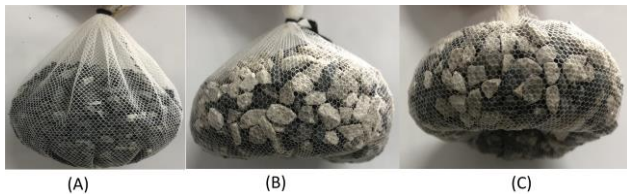


Fig. 1 (A) N-type, (B) S-type & (C) RU.

Previous studies highlighted that S-type FU is quite difficult to deform compared with N-typed FU, and stacking arrangement of S-type FUs is more stable than single layer layout<sup>2)</sup>. However, N-type FU can adapt perfectly into any space where the construction is required.

In this study, we have carried out two types of hydraulic model experiments: "single-FU" experiment and "multiple-FU" experiment. In the former experiment, various types of FUs are tested one by one with the scale of 1/35 to study sliding mechanism of each FU, and to compare stability of the FU. Based on the experimental results, an optimum FU is selected for multiple-FU experiment. The multiple-FU experiment (scale 1/40) is then carried out on the sloping breakwater in planar arrangement in order to evaluate the stability coefficient of optimum FU.

## 2. Outline of Hydraulic Model Experiments

### 2.1 FU Models

Two groups of restricted type (S-type FU), by changing the volume ratio of filter net to filling material and constraining rope length and normal type (N-type FU) as well as Rock Unit (RU) were used in the first experiment. All these FUs have the same mass, 186.5 g, and also same volume (approximately) of filling material, but different volumes of filter net.

The particulars of S-type FU models for the single-FU experiment, that are considered based on the FUs applied in several practical cases, are as shown in Table 1 & 2.

Table 1 S-type FUs changing in filter net size.

Case A	Width x Length (mm x mm) of Filter Net	Constraining Rope Length (mm)
A1	200 x 120	28
A2	240 x 120	28
A3	260 x 120	28
A4	280 x 120	28
A5	320 x 120	28

Table 2 S-type FUs changing in constraint degree.

Case B	Width x Length (mm x mm) of Filter Net	Constraining Rope Length (mm)
B1	260 x 120	18
B2	260 x 120	28
B3	260 x 120	38

### 2.2 Experimental Set-up and Test Conditions

All tests were conducted in a 30 m-long, 0.71 m-wide, and 1 m-deep wave flume of Osaka University. The tests in both experiments were started with small amplitude waves which did not cause any movement of FU, and the wave height was gradually increased until the FU show movement due to the striking wave. The height of the striking wave was increased gradually without rearranging the FU and without rebuilding the rubble mound slope.

#### 2.2.1 Single-FU Experiment

The FU movement was defined as a damage when a portion of FU has moved in to the lee side of the rubble mound slope. These experimental cases were conducted under regular waves on the surface of fixed rubble mound. The test procedure was repeated three times to confirm critical wave height of each FU. The experimental set-up in the wave flume is given in Fig. 2.



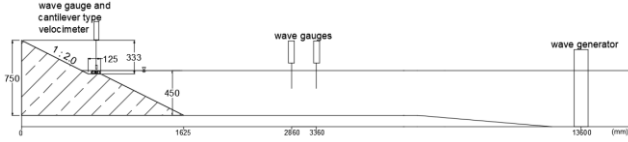


Fig. 2 Experimental set-up of single-FU experiment.

### 2.2.2 Multiple-FU Experiment

In these test cases, FU damage was defined when a FU had moved more than half of its diameter from its initial position. The experimental set-up of these experiment cases are as shown in Fig. 3 and the test conditions are given in Table 3.

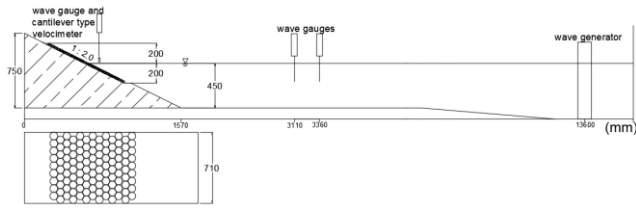


Fig. 3 Experimental set-up of multiple-FU experiment.

Table 3 Test conditions of multiple-FU experiment.

Scale	1/40
Water depth	45 cm
Irregular Waves	Modified Bretschneider Spectrum
Wave period $T_{1/3}$	1 sec, 1.5 sec, 2 sec
Wave height $H_{1/3}$	6cm-10cm
Number of waves	1000
FU model: mass	125 g

### 3. Hudson's Formula

The stability of a particular shore protection unit can be described by the Hudson's Formula (1),

$$K_D = \frac{\rho_r H^3}{M \left( \frac{\rho_r}{\rho_w} - 1 \right)^3 \cot \theta} \quad (1)$$

Where,  $K_D$  and  $M$  are stability coefficient and mass of armor unit;  $\rho_r$  and  $\rho_w$  are density of armor unit and density of water;  $H$  is design wave height; and  $\theta$  is angle of structure slope measured from horizontal in degrees. This formula was developed through the results of extensive small scale model testing and some preliminary verifications of large scale model testing to determine the stability of armor units on rubble structure.

### 4. Experimental Results

#### 4.1 Single-FU Experiment

The movement of all FUs was measured in both horizontal and vertical plane, and the critical wave heights that caused the damage as per the definition were investigated. The critical wave height results in both cases A & B are as shown in Fig. 4 & 5.

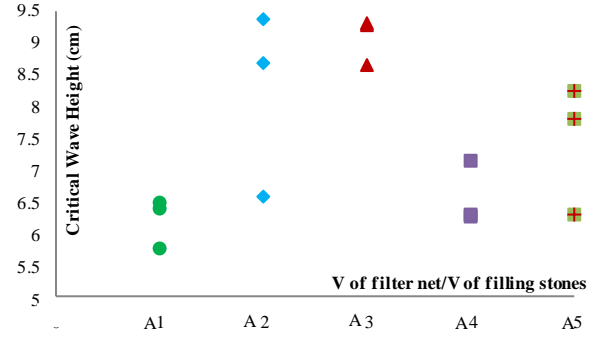


Fig. 4 Comparison of critical wave heights in Case A.

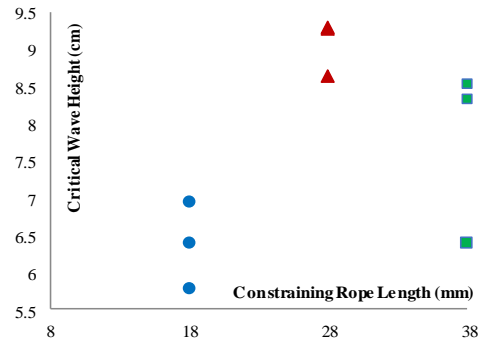


Fig. 5 Comparison of critical wave heights in Case B.

The critical wave heights of N-type FU and the Rock Unit were lower than that of Case A3/B2. Thus it was selected as the optimum FU for the next experiment.

The sliding mechanism of the Rock Unit followed a linear motion, and N-type FU moved by deforming. Some of S-type FUs turned over during the wave attack.

#### 4.2 Multiple-FU Experiment

The optimum FU, selected from the first experiment, was subjected to irregular waves in these experiment cases. The number of FUs, which had moved more than half of its diameter, was recorded with the significant wave height for all tests of wave periods, 1 sec, 1.5 sec and 2 sec. The structure damaged severely for waves with longer periods.

### 5. Conclusions

From the first experiment, it had found that the critical wave height (stability) of S-type FUs depends on the volume ratio of the filter net to filling stones as well as on the constraint degree, and the Case A3/B2 is the most effective FU structure among all FUs tested. The stability coefficient of the FU is quite large compared with other armor units, which indicates that an FU is suitable in practical use from the viewpoint of structure stability.

#### References

- 1) Shin-ichi Kubota et al, Stability and Durability of Filter Unit for Protecting Rubble Mound of Composite Breakwater, Coastal Structures 2007, Vol.2.
- 2) Yuki Saito, The Stability of Filter Units on a Slope of Composite Breakwater, 2017

# Experimental Study on a Strengthening Technique by Wing Walls for Flat Plate-Column Connections with Low-Strength Concrete

Samdani H M Golam

Concrete Structure Laboratory, Department of Architectural Engineering

**Key Words:** Brick chips, Half scale test, Punching shear failure, Retrofitting, Wing walls

## 1. Introduction

A reinforced concrete (RC) flat plate structural system is a structurally economic and feasible system. However, it is prone to show brittle punching shear failure at the flat plate-column connections, which may lead in the progressive collapse of a building. This study focuses on the strengthening of flat plate-column connections in existing structures made with low-strength concrete built in Bangladesh. Because of unexpected increase in applied loads, lack of consideration of seismic effects, and inappropriate management during design and/or construction, a significant number of existing flat plate structures are currently required to be strengthened against punching shear failure. Therefore, the seismic evaluation and retrofit methods are necessary to be developed. This study proposes a new strengthening technique using RC wing walls and describes a series of experimental investigations on the behavior of half-scaled flat plate-column connections.

## 2. Experimental Program

### 2.1 Material properties

Experimental research on a series of three half-scaled interior slab-column connections was conducted mainly to investigate the effectiveness of the proposed retrofit technique using wing walls and the punching shear capacity of the connections with low strength concrete. Two specimens, FP-W1 and FP-W2 were retrofitted by wing walls. Another specimen (specimen FP-1<sup>1)</sup>) was tested without wing walls and served as a control specimen to make comparison between the cases with and without retrofitting.

Wing walls were attached along the longitudinal direction for specimen FP-W1, while the direction was along with the transverse

direction for specimen FP-W2.

The specimen details are shown in Fig. 1. The plate dimensions were 1500 x 1100 x 75 mm in length x width x thickness, respectively. The dimensions of wing walls were 175 x 100 mm in length x thickness, respectively. Moreover, two steel plates (PL-6 x 80, SS400) were embedded in both sides of the slab, mainly to realize the punching shear failure. Thus, the design ultimate flexural strengths of the plate and column were sufficiently larger than the punching shear strength. The material properties of concrete and reinforcements are shown in Table 1 and Table 2, respectively. A cement and CaCO<sub>3</sub>: sand: brick chips volumetric ratio was designed as 1 (0.7+0.3): 2: 4, where 30% of cement was replaced by CaCO<sub>3</sub> mainly to reduce the concrete strength. A ratio of water to the sum of cement and CaCO<sub>3</sub> was 60%.

Table 1 Material properties of concrete

Type	Compressive strength (N/mm <sup>2</sup> )	Elastic modulus (N/mm <sup>2</sup> )	Strain at compressive strength ( $\mu$ )
FP-1	6.93	8,450	1,829
FP-W1	7.16	8,672	1,694
FP-W2	7.20	8,741	1,586
Wing walls	37.04	30,929	1,956

Table 2 Material properties of reinforcements

	Yield stress (N/mm <sup>2</sup> )	Elastic modulus (N/mm <sup>2</sup> )	Tensile strength (N/mm <sup>2</sup> )
D6 (SD295A)	381	191,000	505
D16 (SD345)	369	175,000	536

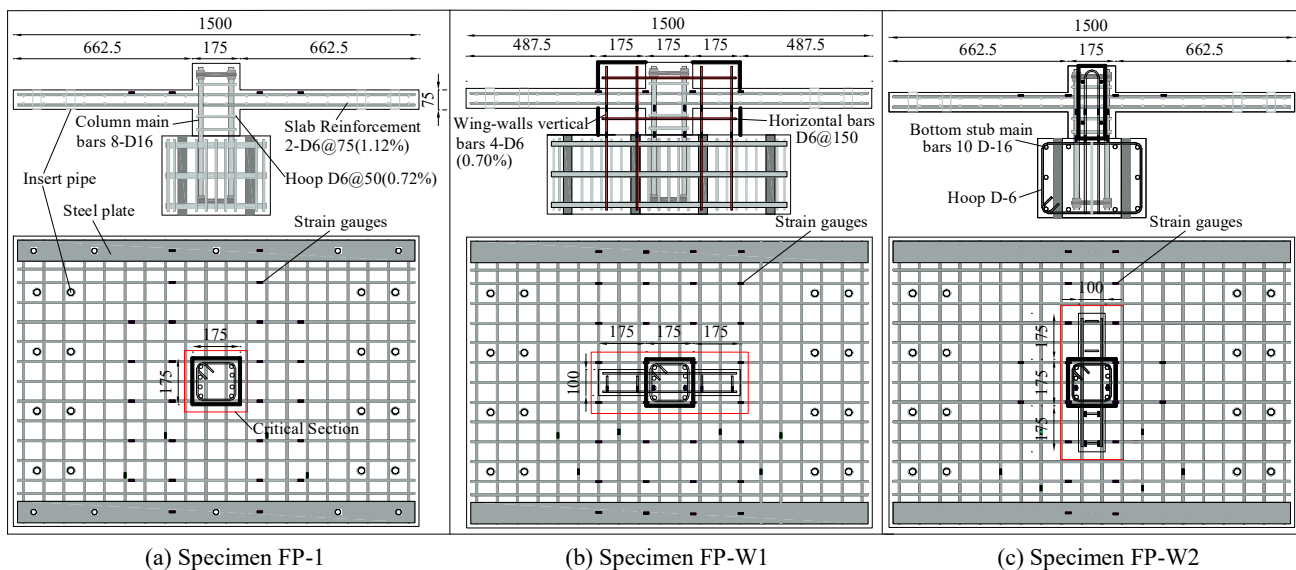


Fig. 1 Details of specimens (Unit mm)

## 2.2 Loading and measurement method

Fig. 2 shows an experiment set-up. The specimens were subjected to static cyclic vertical loads by two hydraulic jacks. The loading was controlled by a drift angle, which was the ratio of vertical displacement from the application point of load to the center of column.

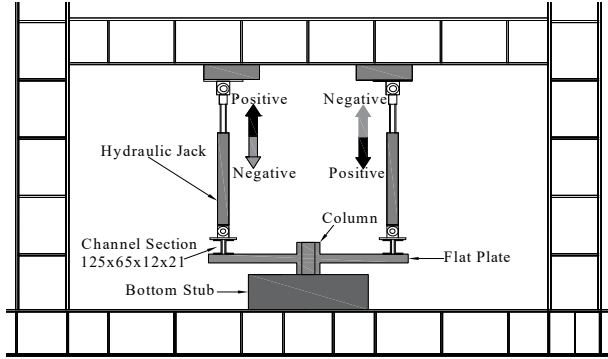


Fig. 2 Schematic view of experiment set-up

## 3. Experimental Results and Discussion

The nodal moment vs vertical drift angle relationships of the specimens are shown in Fig. 3. Specimen FP-1 was tested as a control specimen. Shear cracks extended radially from the column and the surface concrete peeled up due to punching shear failure. Punching was fully visible at  $R$  of  $3.34 \times 10^{-2}$  rad.

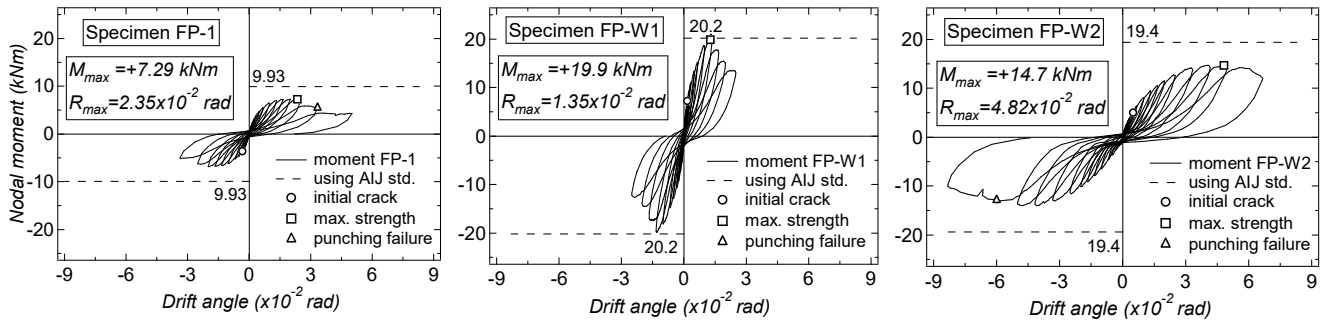


Fig. 3 Nodal moment vs drift angle relationship

Specimen FP-W1 showed higher strength but did not experience higher deformation capacity. The strength decreased with raising up of the surface concrete due to punching shear failure. The punching shear failure was visible at the peak loads of both positive and negative loading at  $R$  of  $1.35 \times 10^{-2}$  rad.

Specimen FP-W2 showed higher strength and deformation capacity than that of the control specimen. The strength decreased with the increase of drift after the peak load. Two slab reinforcement in the connection between slab and wing walls were yielded at peak load. Punching shear failure was fully visible at  $R$  of  $-6.0 \times 10^{-2}$  rad on the bottom surface of the slab.

## 4. Ultimate Strength Evaluation

The experimental ultimate strengths are compared to the design calculations, as shown in Table 3. The flexural strength of the plate was calculated by the following equation<sup>3)</sup>:

$$M_y = 0.9 \sum a_{t1} \sigma_{y1} d_1 + 0.9 \sum a_{t2} \sigma_{y2} d_2 \quad (1)$$

The punching shear strength  $M_0$  was calculated according to the following equations by the AIJ standards for RC structure<sup>3)</sup>:

$$M_0 = M_f + M_s + M_t \quad (2)$$

where symbols and details of the above equations (1) and (2) can be referred to the reference<sup>2,3)</sup>.

Table 3 Experimental and calculated strengths

	Strength	FP-1	FP-W1	FP-W2
Max. capacity	$M_{exp}$ (kNm)	7.3	19.9	14.7
Flexural strength	$M_y$ (kNm)	25.1	25.1	25.1
Punching shear strength	$M_f$ (kNm)	3.56	3.48	8.72
	$M_s$ (kNm)	2.71	6.9	6.92
	$M_t$ (kNm)	3.66	9.84	3.73
	$M_0$ (kNm)	9.93	20.2	19.4

The maximum capacity of FP-W1 was 2% lower than the calculated result of the punching shear strength, whereas 27% lower for FP-1 and 25% lower for FP-W2. In particular, the equations for punching shear strength provided by the AIJ standards overestimated for all specimens, which might be caused by application of low-strength concrete.

## 5. Conclusions

From the experimental results explained above, the following conclusions were obtained:

- 1) The maximum strengths of both strengthened specimens were significantly increased compared to that of the control specimen. Moreover, the ductility of the specimen FP-W2 was

larger than that of the specimen FP-W1.

- 2) Punching shear failure occurred in the specimens. Shear cracks extended radially from the column or wing walls surfaces and the slab surface concrete peeled up due to punching shear failure.
- 3) The punching shear strengths calculated based on the AIJ standards overestimated for all specimens.
- 4) It was experimentally verified that installing RC wing walls was a feasible method of upgrading flat plate-column connections under seismic loading conditions.

## References

- 1) H M Golam Samdani, Seolmi Kim, Susumu Takahashi, Suguru Suzuki, Yasushi Sanada: AIJ Annual Convention, Vol.4, pp.445-446, 2018.
- 2) Seolmi Kim, H M Golam Samdani, Susumu Takahashi, Suguru Suzuki, Yasushi Sanada: AIJ Annual Convention, Vol.4, pp.447-448, 2018.
- 3) Architectural Institute of Japan: AIJ Standard for Structural Calculation of Reinforced Concrete Structures revised 2010, 2014.9 (in Japanese).

# Development of an Influence Coefficient Database for Evaluating Mixed-mode SIFs and Application to Inclined Surface Cracks in Semi-infinite Bodies

PHYO MYAT KYAW

Ocean Material Engineering Lab., Naval Architecture and Ocean Engineering Department

**Key Words:** influence function method, mixed-mode SIFs, crack face traction, inclined surface cracks, FEM

## 1. Introduction

Accurate estimation of stress intensity factors (SIFs) is a critical factor in improving the reliability of evaluated fatigue crack propagation rates for ship and offshore structures. By using the influence function method (IFM)<sup>1)</sup>, SIFs for cracks under arbitrary stress fields can be easily calculated. Previous studies of IFM described the evaluation of mode-I SIFs and mixed-mode SIFs (MM-SIFs)<sup>1-4)</sup> without crack face traction (CFT) which can improve the accuracy of SIF solutions.

In this study, an effective technique is proposed to compute MM-SIFs for inclined surface cracks in semi-infinite bodies under arbitrary stress fields by means of IFM considering the CFT<sup>5-7)</sup>. The accuracy and effectiveness of the developed influence coefficient database (ICDB) and proposed technique is verified with well-established reference solutions<sup>7-9)</sup>. The effect of Poisson's ratio on MM-SIFs is also discussed based on the evaluated MM-SIF solutions.

## 2. Theoretical background

The IFM proposed by Shiratori et al.<sup>1)</sup> is based on superposition principle and finite element analysis (FEA). The six components of stresses,  $\sigma_{ij,p}$ , at  $P$ -th node which is located on the crack face of the non-cracked medium are evaluated under given external loading by means of FEA.

MM-SIFs at the crack front node,  $Q$ -th node,  $K_I^{ij,PQ}$ ,  $K_{II}^{ij,PQ}$  and  $K_{III}^{ij,PQ}$ , due to unit distributed load (UDL) at the  $P$ -th node are then evaluated. The interaction integral method (IIM) considering the CFT integral<sup>5-7)</sup> is employed in the evaluation of MM-SIFs due to the UDL. The IIM given in WARP3D code is modified so that six components of traction stresses can be applied at each node on the element face of the crack face. The calculated MM-SIFs, are called influence coefficients (IC). The values of IC for each node on the crack face are then saved to a database, called ICDB.

According to the IFM, MM-SIFs at the  $Q$ -th node on the crack front,  $K_I^Q$ ,  $K_{II}^Q$  and  $K_{III}^Q$ , can be calculated as in Eq. (1).

$$\begin{cases} K_I^Q = \sum_P K_I^{ij,PQ} \sigma_{ij,P} \\ K_{II}^Q = \sum_P K_{II}^{ij,PQ} \sigma_{ij,P} \\ K_{III}^Q = \sum_P K_{III}^{ij,PQ} \sigma_{ij,P} \end{cases} \quad (1)$$

## 3. Proposed Technique

By Saint-Venant's principle (SVP), when a body is large enough, the MM-SIFs for a non-inclined crack subject to this multiaxial CFT stresses are nearly equal to those of the inclined crack subject

to the remote uniaxial stress. These lead to an assumption that the MM-SIFs of a non-inclined crack in a large body subject to the multiaxial CFT stresses, which occur on the inclined crack face under the uniaxial loading, should be the same as those of an inclined crack in a semi-infinite body subject to the remote uniaxial stress. Based on this assumption, a technique is proposed to calculate MM-SIFs accurately for surface cracks in semi-infinite bodies subject to a remote stress with different crack orientations in short time and with no effort for generating many finite element (FE) models.

The traction stresses induced on the crack face of the inclined crack model can produce MM-SIFs. The applied traction stresses on the inclined crack face were transformed in accordance with the crack angle.

The traction stresses for any crack angle can be readily transformed, for example, by using the Microsoft spread worksheet. By employing the proposed technique, only one FE model with a non-inclined crack can be used for calculating MM-SIFs for any crack angle based on the transformed traction stresses. Based on that, MM-SIFs for cracks with different angles in semi-infinite bodies and subject to arbitrary stress distributions can be readily calculated using a non-inclined cracked model by means of the proposed technique. This technique efficiently reduces the man-hours needed to generate FE model and traction stresses as well as it accurately evaluates MM-SIFs for different crack angles.

## 4. Numerical Examples

Four different numerical analyses are conducted for this study. The first two analyses validate the adequacy of the IFM based MM-SIF calculation system which is to be employed in the proposed technique. The proposed technique is then validated. Finally, MM-SIFs for different crack angles and Poisson's ratios are evaluated.

### 4.1 Model definition

The target FE models used in the numerical examples are chosen to be large enough so that they can be treated as the semi-infinite bodies based on the assumption of SVP. The semi-infinite bodies are needed to be employed in the proposed technique so that different load directions and crack angles can be included in the analyses. In the validation of ICDB for semi-infinite bodies, the flat plate surface-cracked models which are subjected to external uni-axial tensile loading for mode-I case and pure shear loading for mixed-mode case are employed.

To validate the proposed technique described in section 3, semi-infinite flat plate models with inclined and non-inclined surface cracked models are used. And then, by means of proposed technique, MM-SIFs for different crack angles are evaluated by using the non-inclined cracked model. Only one FE cracked model



with a non-inclined crack is employed for all the applied crack angles. Fig. 1 shows the geometric configuration of one of the flat plate surface-cracked models used in this study.

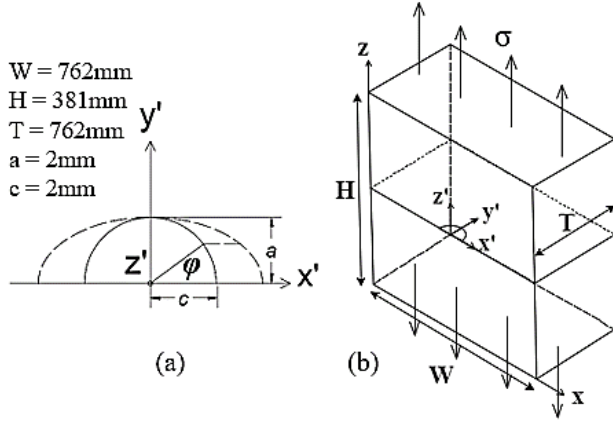
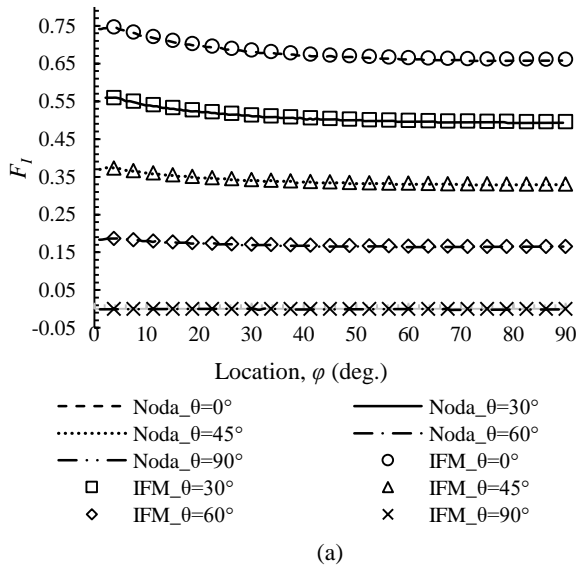


Fig. 1 A semi-circular surface crack in a semi-infinite flat plate body. (a) geometry of the crack face and (b) geometry of the cracked body.

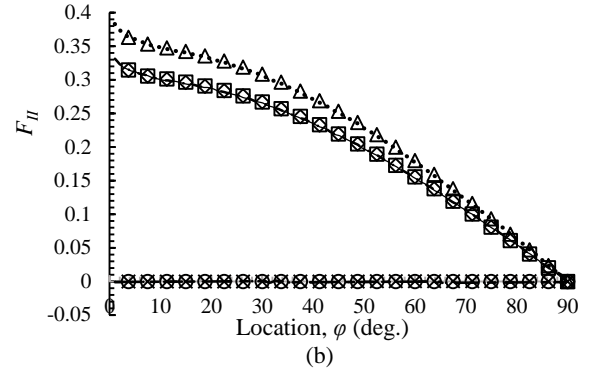
#### 4.2 Results and discussion

The calculated SIFs for the above-mentioned FE models are compared with well-established reference solutions<sup>(7-9)</sup> where an excellent agreement was achieved. Fig. 2 shows the calculated MM-SIFs for different crack angles by means of the proposed technique in comparison with the reference solutions<sup>(9)</sup>. The solutions obtained by means of the IFM are described as 'IFM'. The reference analytical solutions<sup>(9)</sup> are denoted as 'Noda'.

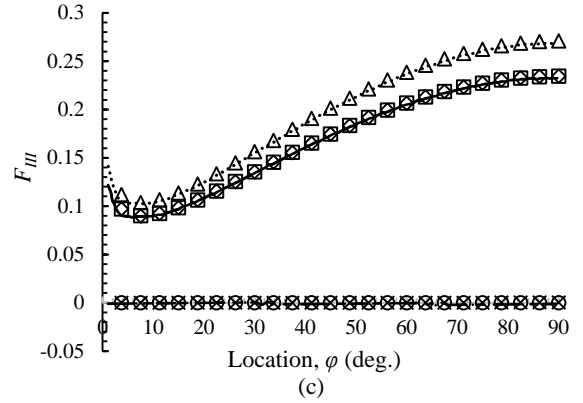
The calculated MM-SIFs are normalized as:  $F_I = K_I^Q / \sigma \sqrt{\pi a}$ ,  $F_{II} = K_{II}^Q / \sigma \sqrt{\pi a}$  and  $F_{III} = K_{III}^Q / \sigma \sqrt{\pi a}$ , where  $F_I$ ,  $F_{II}$  and  $F_{III}$  denote normalized mode-I, -II and -III SIFs while  $K_I^Q$ ,  $K_{II}^Q$  and  $K_{III}^Q$  are calculated mode-I, -II and -III SIFs. The locations along the crack front are represented by  $\phi$  (in degrees) in which  $\phi = 0^\circ$  denotes the crack mouth and  $\phi = 90^\circ$  represents the crack deepest point.



(a)



(b)



(c)

Fig. 2 Validation of MM-SIF solutions for different crack angles,  $a/c = 1.0$ ,  $\nu = 0.3$ . (a)  $F_I$ , (b)  $F_{II}$  and (c)  $F_{III}$ .

#### 5. Conclusions

The following facts can be concluded for the present study.

- 1) ICDB of cracks in semi-infinite bodies is constructed and validated by using FE models of cracked bodies which are large enough compared to the crack size based on the assumption of SVP.
- 2) The new proposed technique works well to evaluate the MM-SIFs for different crack angle with single FE model. It also reveals the effectiveness and handiness for numerical analyses of different crack angles without consuming time for FE modelling.
- 3) In this study, wide range of MM-SIFs for different aspect ratios and Poisson's ratios which are not described in previous studies is also calculated and presented.

#### References

- 1) Shiratori M et al.: T of JSME, Vol.52, pg. 390–8, 1986. (in Japanese)
- 2) Shiratori M et al.: T of JSME, Vol.56, pg. 265–71, 1990. (in Japanese)
- 3) Shiratori M et al.: ASME, Vol. 6, pg. 929–39, 2011.
- 4) Osawa N et al.: J of JASNAOE, Vol.12, pg. 201–8, 2010. (in Japanese)
- 5) Gadallah R et al.: J of Ocean Eng., Vol.138, pg. 123–39, 2017.
- 6) Gadallah R et al.: J of EFM, Vol.197, pg. 48–65, 2018.
- 7) Gadallah R et al.: J of ASME, Vol.3, 2016,
- 8) Noda N et al.: J of IJF, Vol.75, pg. 19–48, 1996.
- 9) Noda N et al.: J of IJF, Vol.127, pg. 167–91, 2004.

# Numerical Calculation Method for Hydroelastic Response of a Ship with Forward Speed in Waves Using Orthogonal Mathematical Mode Function

Hong Yang

Ocean Space Development Laboratory, Department of Naval Architecture and Ocean Engineering

**Key Words:** Hydroelasticity, Rankine panel method, Mode functions, Orthogonal polynomials, Frequency domain

## 1. Introduction

In recent years, larger merchant ships are built due to the increase in ocean transport. As the size of ships increases, ships become more flexible and associated accident is liable to occur. Therefore, to compute wave-induced hydroelastic responses with sufficient accuracy becomes of engineering importance. In particular, wave-induced vibrations, referred to as springing and whipping, can aggravate the fatigue damage of very large ships.

In structural analysis, it is common to define a special set of natural mode shapes, which correspond to the actual flexural deflections of the body in a specified physical context. Sometimes this may be difficult in hydroelastic problems because the mode shapes must satisfy the edge boundary conditions and they are affected by the hydrodynamic pressure field and hence cannot be specified in advance. This difficulty can be avoided if the structural deflection is represented instead by a superposition of simpler orthogonal mathematical mode shapes which are sufficiently general and complete to represent the physical motion.

In the present study, the structural deflections of a floating slender ship can be expressed by the free undamped ‘wet’ bending modes of the hull in the water, by the ‘dry’ modes of the same structure in air, or more simply the orthogonal modes of a uniform beam. An even simpler representation can be developed in terms of orthogonal polynomial mathematical functions, despite the fact that these lack a physical basis and do not satisfy the appropriate free-edge boundary conditions<sup>1)</sup>. This research is directed to prove that a superposition of orthogonal mathematical functions can represent the flexural deflection of a ship in waves, despite of the required boundary conditions, and the advantages and disadvantages of orthogonal mathematical functions are discussed.

## 2. Numerical Calculation Method

### 2.1 Mode functions

There are two mode functions applied in this research to present the deformation of the elastic body. The first is natural modes using Euler-Bernoulli's free-free beam, which satisfies boundary conditions and is used commonly. The another is Legendre polynomial modes despite the fact that lack a physical basis. An especially compact expression for the Legendre polynomials is given by Rodrigue's formula:

$$P_n(q) = \frac{1}{2^n n!} \frac{d^n}{dq^n} (q^2 - 1)^n \quad n = 0, 1, 2, \dots \quad (1)$$

There two mode functions are both orthogonal, and the illustration of mode shapes of these modes are shown as Fig. 1.

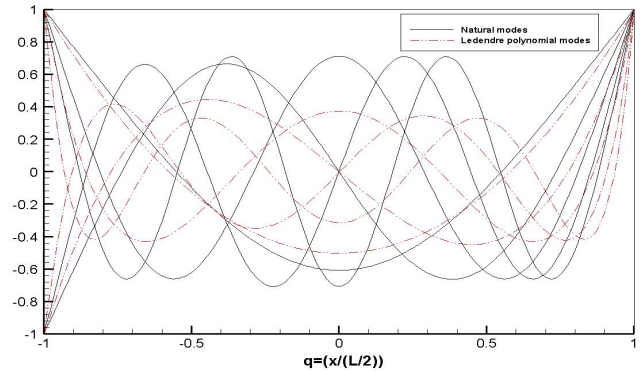


Fig. 1 Mode shapes of Euler-Bernoulli's beam and Legendre polynomials in vertical bending.

### 2.2 Response function

The response function given from beam equation<sup>2)</sup> is shown in Eq.(2).

$$\sum_j [-\omega^2 (M_{ij} + a_{ij}) + i\omega b_{ij} + C_{ij} + D_{ij}] X_j = E_i \quad (2)$$

### 2.3 Mass matrix and stiffness matrix

The mass matrix and stiffness matrix in above equation can be calculated as

$$M_{ij} = \int_{-L/2}^{L/2} m f_i(x) f_j(x) dx \quad (3)$$

$$D_{ij} = \int_{-L/2}^{L/2} EI f_i''(x) f_j''(x) dx \quad (4)$$

and both matrices are symmetric matrices.

## 3. Computational Results

### 3.1 Hydrodynamic analysis based on frequency domain RPM

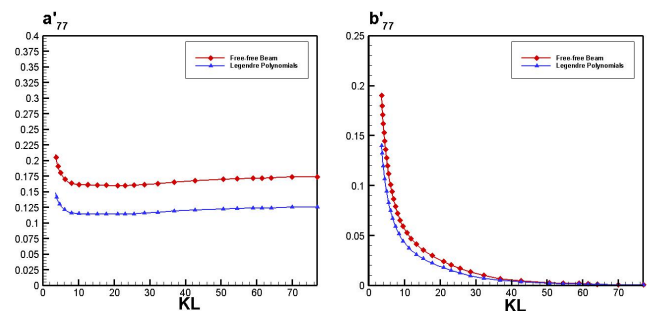


Fig. 2 Added mass and damping coefficient of the first bending mode.

Fig.2 shows the computed results of the non-dimensional

added mass and damping coefficient. The differences of these between alternative mode functions can be noticed but the tendencies is at the same pace.

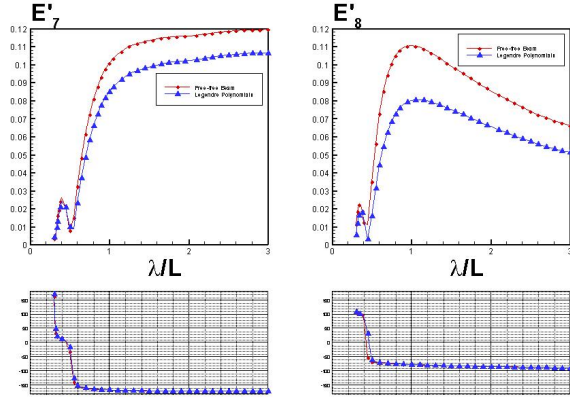


Fig.3 Exciting force of the first and second bending mode.

The tendency of amplitude of each bending mode is at same pace but the phase could be almost same from Fig.3.

The differences between two mode functions exist surely because the magnitude of natural modes is slightly larger than Legendre polynomial modes shown in Fig.1.

### 3.3 Amplitudes of ship motions

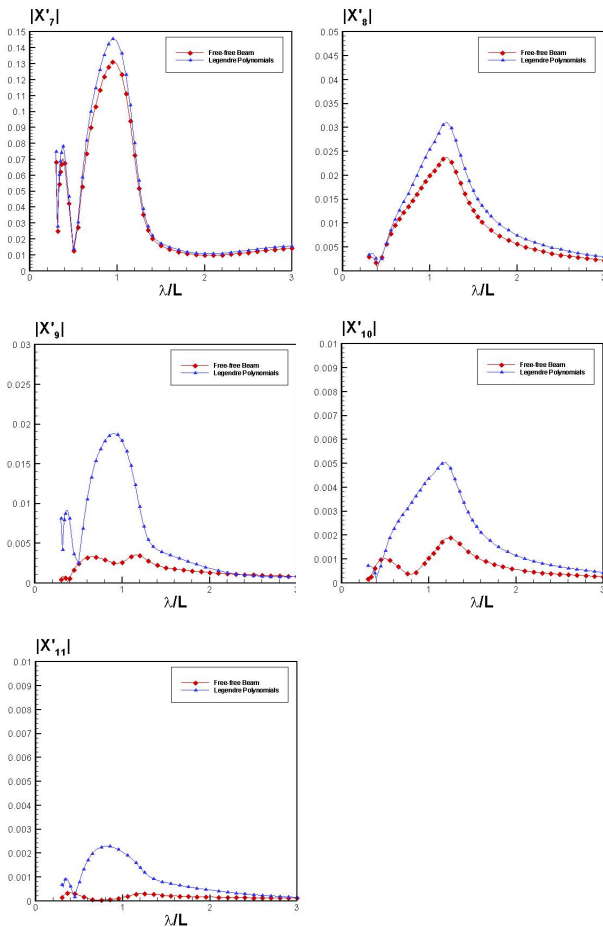


Fig.4 Ship motions of the first five bending modes.

Conversely, in Fig.4, the ship motions of the first five bending modes using Legendre polynomial modes are much

larger than natural modes.

In this research, it is the total elastic deformation rather than the amplitude of each bending mode that should be forced on. For find out the convergence numbers of each mode we need, the several values are defined as Eq.(5).

$$|X'_{sj}| = \left| \sum_{i=7}^{7+j} X'_i \right| \quad (5)$$

The results of j from 1 to 4 are illustrated in Fig.5

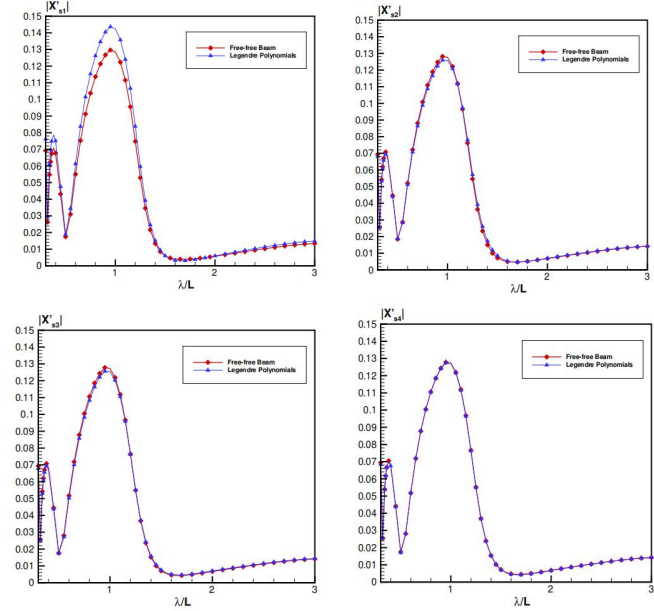


Fig. 5 Ship motion summations of several bending mode.

From Fig.5, we can find good agreement is observed as well in this comparison as long as enough bending modes added, despite of the difference existed in hydrodynamic force and lacking physical meanings.

## 4. Conclusions

In this paper, the hydrodynamic force is computed using different mode functions, and there are must difference existed.due to different magnitudes of mode functions.

The Legendre polynomial modes can replace of nature modes using at least five bending modes for precision and in the engineering filed with more complex boundary conditions, Legendre polynomial modes are much more easier without considering any boundary conditions as long as enough bending modes.

## References

- 1) Newman J N. Wave effects on deformable bodies[J]. Applied ocean research, 1994, 16(1): 47-59.
- 2) Bishop R E D, Bishop R E D, Price W G. Hydroelasticity of ships[M]. Cambridge University Press, 197

# Effectiveness and Mechanism of Broaching-To Prevention Using Global Optimal Control (CMA-ES)

Sreenath Maniyappan

Ship Design Subarea, Department of Naval Architecture and Ocean Engineering

**Key Words:** *optimal control, broaching, fixed point stability, unstable invariant manifold*

## 1. Introduction

Broaching-to is a phenomenon in which a ship cannot maintain a constant course despite maximum steering effort. Most experiments and numerical simulations carried out related to broaching, engage PD control. However, in order to realize the concept of the maximum steering effort in broaching, the control system can be improved using the optimal control strategies.

The first effort in this direction using optimal control was done by Maki et al.<sup>3)</sup> in 2008, using the variational method based algorithm known as SCGRA (Sequential Conjugate Gradient-Restoration Algorithm) method and SQP (Sequential quadratic programming) algorithm. However, these techniques were not sufficiently powerful to be used in rugged search landscape. Further, in 2018 Maki et al.<sup>1)</sup> carried out a numerical simulation using a powerful optimization algorithm known as CMA-ES (Covariance Matrix Adaptation-Evolutional strategy)<sup>4)</sup>. Both these attempts showed the capability of optimal control in preventing the broaching phenomenon but physical explanation of this mechanism remains to be investigated.

Hence, in this research we use CMA-ES for optimal rudder control, with an improved rudder model in a 4DoF Surge-Sway-Yaw-Roll maneuvering model. Further, simulate broaching conditions and nonlinear analysis on the system carried out. Subsequently, the effectiveness of optimal control over a range of Froude number and autopilot course are investigated.

## 2. Methodology

### 2.1 CMA-ES

It is a probabilistic model-based and comparison-based algorithm, which does not require differentiability of the objective function that is suitable for simulation-based optimization.

### 2.2 Maneuvering Simulation model

The subject ship is ITTC-A2 a 135 GT purse seiner. I use the 4 DoF surge-sway-yaw-roll model<sup>2)</sup> having the wave trough fixed and ship CoG fixed coordinate systems are being used. The system could be represented using the state vector,  $\mathbf{x}$ , and parameter vector,  $\mathbf{p}$ , as follows

$$\mathbf{x} = \left\{ \frac{\xi_G}{\lambda}, u, v, \chi, r, \phi, p, \delta \right\}^T \quad (1)$$

$$\mathbf{p} = \{n, \chi_c\} \quad (2)$$

where,  $\xi_G$  is the longitudinal position of CoG of the vessel from a wave trough. The dynamical system in case of PD control can be represented by the following state equation.

$$\dot{\mathbf{x}} = \mathbf{F}(\mathbf{x}; \mathbf{p}) = \{f_1(\mathbf{x}; \mathbf{p}), f_2(\mathbf{x}; \mathbf{p}), \dots, f_8(\mathbf{x}; \mathbf{p})\}^T \quad (3)$$

Here  $f_1$  to  $f_8$  are obtained from the equations of ship motions in waves.

### 2.3 Optimal control formulation

The problem is treated as an optimal control case, having specified initial condition and free final condition, with an objective function  $J$  to be minimized.

$$J = \begin{cases} \frac{1}{t_f} \int_0^{t_f} (\chi - \chi_c)^2 dt, & |\phi| < |\phi_v| \\ K, & |\phi| \geq |\phi_v| \end{cases} \quad (4)$$

here  $K$ , is a penalty value to prevent capsizing.

Optimal control is realized in two different ways as follows:

**Method I (Optimal  $\delta$  CMAES):** the state equation (3) is modified by replacing the rudder differential equation with the optimal solutions generated by CMA-ES. This means that steering gear dynamics are ignored.

**Method II (Optimal Rudder gains CMAES-PD):** The state equation for steering gear remains the same with the rudder proportional and differential gains optimized.

### 2.4 Stability Analysis

Firstly, the fixed points  $\bar{\mathbf{x}} = \{\bar{\frac{\xi_G}{\lambda}}, \bar{u}, \bar{v}, \bar{\chi}, \bar{r}, \bar{\phi}, \bar{p}, \bar{\delta}\}$  are obtained by solving the following equation:

$$\mathbf{F}(\bar{\mathbf{x}}; \mathbf{p}) = \mathbf{0} \quad (5)$$

Then evaluating the eigenvalues of Jacobian matrix

$$D\mathbf{F}(\bar{\mathbf{x}}; \mathbf{p}) = \frac{\partial}{\partial \mathbf{x}_j} f_i(\mathbf{x}; \mathbf{p}) \quad 1 \leq i, j \leq 8 \quad (6)$$

If an eigenvalue of equation (6) has a positive real part, local asymptotic behavior at  $\bar{\mathbf{x}}$  is unstable and if the real part of all eigenvalues are negative then local behavior is stable.

## 3. Results

Fig.1 shows the success region for the two different optimal control methods adopted in this research.



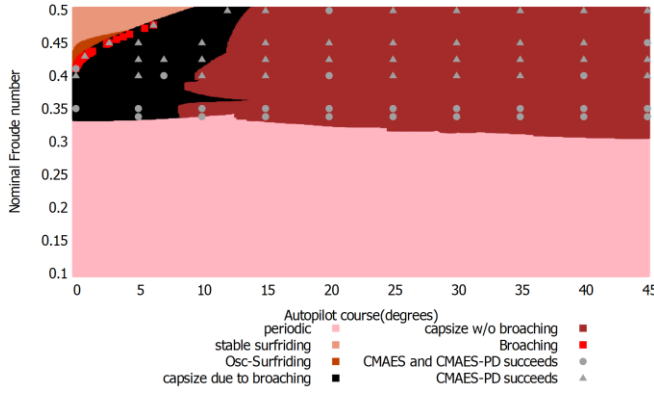


Fig.1 Effectiveness of optimal control in avoiding broaching/capsizing

### 3.1 Mechanism Type 1

$$\frac{\lambda}{L} = 1.637, \frac{H}{\lambda} = 0.1, \chi_c = 5^\circ, Fn = 0.3381$$

Here the conventional PD control results in broaching associated with surf-riding, the optimal control and optimal PD control does in periodic motion as shown in Fig. 2. The slightly larger rudder action around the equilibrium point prevents the ship to touch the unstable equilibrium and the trajectory undergoes a qualitative change, as can be explained using Fig. 3&4.

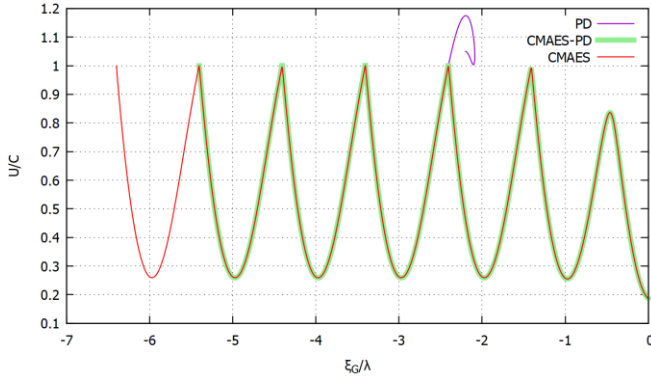


Fig. 2 Phase portrait of surge motion

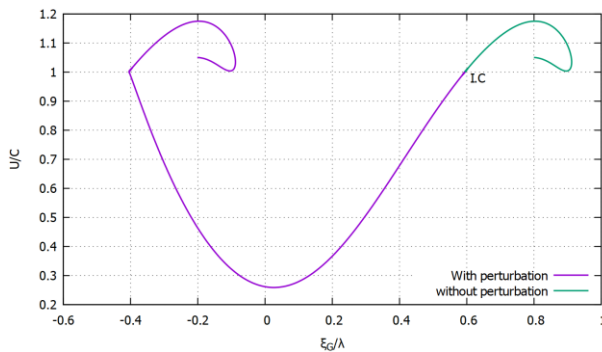


Fig. 3 Unstable Invariant Manifold of the fixed point near wave crest

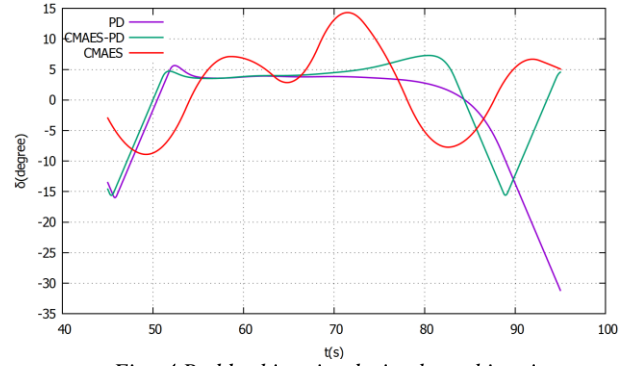


Fig. 4 Rudder histories during broaching time

### 3.2 Mechanism Type 2

$$\frac{\lambda}{L} = 1.637, \frac{H}{\lambda} = 0.1, \chi_c = 0.1^\circ, Fn = 0.35$$

In this case the system instability is weakened by the large differential gain in optimal PD and causes the system to remain in surf-riding for longer duration.

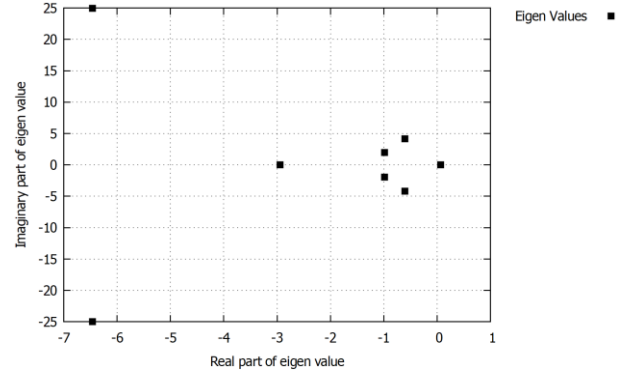


Fig. 5 Eigen value of unstable fixed point under optimal gain

## 4. Conclusion

Two different mechanisms how optimal control avoids broaching are identified. This information could be vital in avoiding dangerous scenarios. The effectiveness of optimal control methods and the dominant mechanisms under varying Froude number and heading angle is also brought out.

## 5. Reference

- 1) Maki, A., Banno, Y., Umeda, N., Sakamoto, N., and Akimoto, Y.: On Broaching-to Phenomenon Using Optimal Control Theory with Evolutional Strategy, Conference proceedings, The Japan Society of Naval Architects and Ocean Engineers, Vol.26, pp.501-506, 2018.
- 2) Umeda, N.: Nonlinear Dynamics of Ship Capsizing due to Broaching in Following and Quartering seas, Journal of Marine Science and Technology, Vol 4, pp.16-26, 1999
- 3) Maki, A., Umeda, N. and Ueno, S., Investigation on Broaching-to Using optimal control theory, Journal of the Japan Society of Naval Architects and Ocean Engineers (In Japanese), Vol.8, pp.115-122, 2008
- 4) Hansen, N.: The CMA Evolution Strategy: A Tutorial. ArXiv e-prints, arXiv:1604.00772v1, 2016

# A numerical study on water environment prediction in L. Kasumigaura using unstructured grid three-dimensional flow model

Wang Yueyi

Water Engineering Laboratory, Department of Civil Engineering

**Key Words:** Unstructured grid, wind driven current, dissolved oxygen, diurnal temperature stratification

## 1. Introduction

Due to temperature difference between inflow river water and lake and the existing of temperature stratification in lakes, inflow rivers can trigger density currents. The different movement patterns of density currents in lakes will directly affect the movement and distribution of nutrients, pollutants or sediment particles, and water quality and ecological environment, then finally has a significant influence on the formation of hypoxia. Hypoxia is not only killing the fishes and invertebrates, but also impacted as an endocrine disruptor and presents a serious danger to the reproduction, hence sustainability of fish populations<sup>1)</sup>. Therefore, it is important to study the characteristics of currents and tempo-spatial change of density in temperature-stratified water for grasping the formation, development and fate processes of surface algae and bottom hypoxia in temperature stratified lakes.

It is very difficult to accurately grasp the flow of lakes only by analyzing the observed data. Consequently, the numerical simulation method should be adopted. Numerical simulation can provide more comprehensive and coherent understanding of the properties of current in the whole area, which makes it possible to precisely analyze phenomena like temperature stratification, hypoxia and so on. The objectives of this study are to verify the applicability of SUNTANS, a recently developed coastal flow model, in Lake Kasumigaura, and then simulate the influence of external forces on variations of current to reveal formation and dispersion characteristics of hypoxia and fate of surface algae. Particle tracking also been used to show the wind driven current on the surface of lake.

## 2. Study Area and Observations

### 2.1 Study Area

Lake Kasumigaura is located in the east-central part of Japan, about 60 km from Tokyo, as shown in Figure 1. Lake Kasumigaura refers to a group of adjacent lakes, can be roughly divided into three parts: Nishiura (西浦; 167.63km<sup>2</sup>), Kitaura (北浦; 35.16 km<sup>2</sup>), and Sotonasakaura (外浪逆浦; 5.85 km<sup>2</sup>), as well as rivers connecting them. The total area is approximately 220 km<sup>2</sup>, which is second largest in Japan. The average depth of the lake is quite small for the large area.

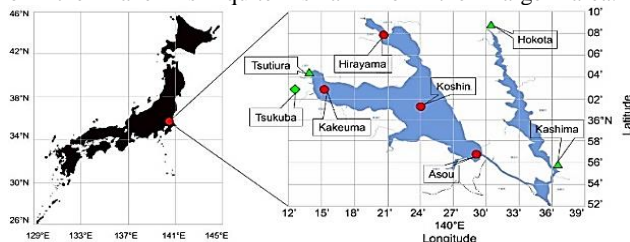


Fig. 1 Location of Lake Kasumigaura and observation stations in the lake area

### 2.2 Observation Data

In Figure 1, red circles marks show the location of observation stations for water quality related data, while the green polygons indicate the location of observation stations for meteorological related data. From observation data, the annual average COD fluctuates around 7mg/L, which is twice as high as environmental standards. At the same time, the concentration of total nitrogen and total phosphorus is about 1.3 mg/L and 0.1 mg/L respectively. That is to say, it exceeds the limit value of eutrophication.

## 3. Calculation Methods

### 3.1 Flow Model

SUNTANS is an unstructured grid, non-hydrostatic, parallel computing coastal ocean model, created by Fringer<sup>2)</sup>. It has been developed for non-hydrostatic simulation of flows at high resolution in estuaries and coastal sea<sup>3) 4)</sup>, while most application uses with hydrostatic condition. Compared with widely used structural grids, unstructured grids have better geometric fitness. This is an important advantage for lakes with complex planar shapes like Lake Kasumigaura. On the other hand, SUNTANS was designed to use Cartesian coordinate system, which could avoid horizontal gradient errors which might be sometimes occurred in sigma coordinate system. With these superiorities, SUNTANS has been chosen as a powerful tool to simulate and also used in this study to analyze the feature of Lake Kasumigaura. SUNTANS uses Boussinesq approximation and incompressibility assumption to solve the Reynolds average Navier-Stokes equation. The horizontal and vertical eddy viscosities are given by Smagorinsky model and Mellor-Yamada turbulent closure model, respectively.

### 3.2 Model Setup

This study followed the approach of Guillaume and Wells<sup>5)</sup> who studied the influence of a typhoon on gyre generation in Lake Biwa, Japan. As for the grid, SMS, a software to generate grids, was also used. Table 1 shows model setup. In order to understand the effects of various external forces, several calculation cases were run with different idealized forcing conditions, as shown in Table 2.

Table 1 Calculation condition

Grid size	Horizontal Average Interval: 200m Vertical: 20 layers	
Calculation period	2010/9/1-2010/9/31	
Input data	Precipitation, atmospheric temperature, wind speed and direction, short wave, air pressure, humidity and cloud conditions.	
Boundary condition	Inflow	4 major rivers
	Outflow	The Hitachi tone river
Initial condition	Water temperature	

Table 2 Forcing scenarios of Lake Kasumigaura simulation

	Inflow	Insolation	Wind
Base Case	○	○	○
Case-1	○	○	
Case-2	○		○
Case-3		○	○

## 4. Results and Discussion

### 4.1 Model Verification

Figure 2 shows the evaluation of simulation results in the base case at all four stations. It can be seen that the calculated results have good consistency. Root mean square errors (RMSEs) of temperature were 0.51, 1.13, 0.56, and 0.91, at the Kakeumaoki, Hirayama, Koshin, and Asou stations, respectively. These results show model has enough prediction skill and still have a potential for improvement, especially in representation of vertical stratification and its diurnal change.

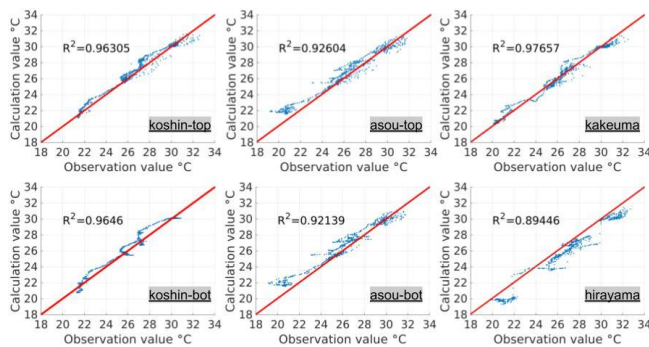


Fig. 2 Comparison of model and observations.

### 4.2 Results

Figure 3 shows the temporal change of temperature during the calculation period in the 4 cases. Red and blue lines indicate surface and bottom temperature, solid and dashed lines are the calculation results and the observations, respectively. Figure 4 shows the results of particle tracking to illustrate the wind-driven effect on motion of surface materials.

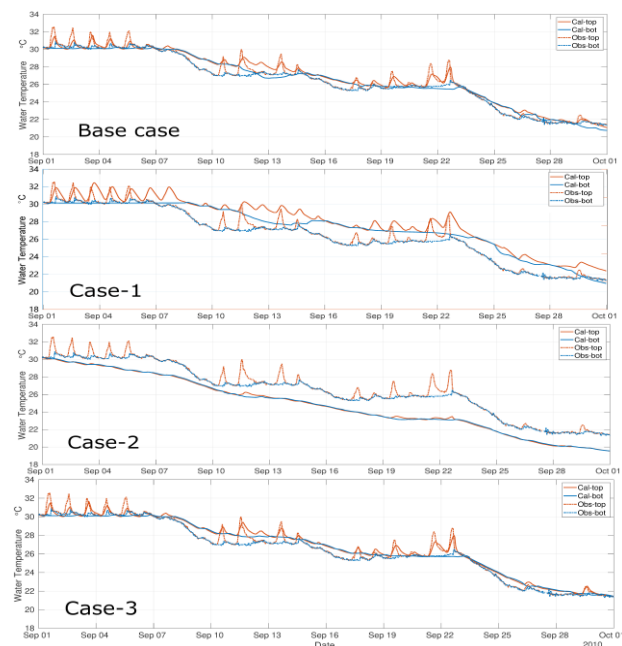


Fig. 3 Comparisons between calculated and observed values of four cases at the Koshin station.

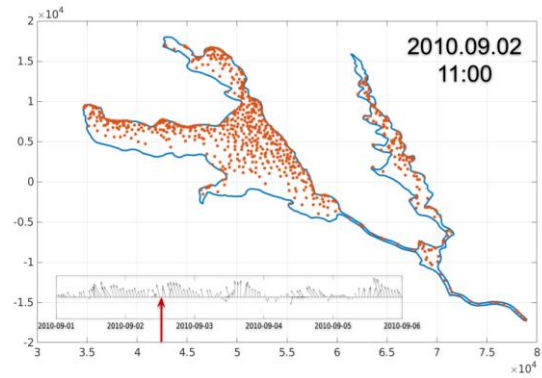


Fig. 4 Particle tracking result at about 11:00 on September 2. The wind chart with red lines marking the time points.

By comparing the cases in Fig. 3, the temperature differences between surface and bottom layers is greater in Case-1, which shows the effect of wind encouraging surface heat exchange. In the case without insolation (Case-2), there is almost no temperature stratification, which indicates that solar radiation plays an important role in the formation of temperature stratification. Case-3 combined with the initial setting of inflow water temperature can also indicate that inflows has a certain effect on water temperature distribution, which is inversely proportional to the distance between the location and the inflow entrance. Figure 4 shows the surface particles like algae move to the north shoreline by the prevailing south wind, resulting in a strong correlation between surface flow and wind.

## 5. Conclusions and Future Plan

The calculated results show a good performance for the obvious diurnal stratification. With evaluation indices it could be said that SUNTANS can maintain reproducibility in the lake region as well as application in coastal and estuarine areas. Through the comparison of results, we have preliminarily grasped the driving effect of wind, the great contribution of insolation to temperature stratification and the importance of correct setting of inflow conditions. Particle tracking simulation can provide a suitable tool for revealing current flow effect on the material cycles.

In order to furthermore investigate the specific causes and characteristics of water blooms and hypoxia in this lake, it is necessary to add the feature of aquatic plants into an ecological model, and then couple with SUNTANS to achieve higher reproducibility in biogeochemical simulation.

### References

- 1) Doudoroff P, Shumway D L. Dissolved oxygen requirements of freshwater fishes[J]. 1970.
- 2) Fringer O B, Gerritsen M, Street R L. An unstructured-grid, finite-volume, nonhydrostatic, parallel coastal ocean simulator[J]. Ocean Modelling, 2006, 14(3-4): 139-173.
- 3) Chua VP, Fringer OB (2011) Sensitivity analysis of three-dimensional salinity simulations in North San Francisco Bay using the unstructured grid SUNTANS model. Ocean Model 39(3):332-350
- 4) Rayson MD, Gross ES, Fringer OB (2015) Modeling the tidal and sub-tidal hydrodynamics in a shallow, micro-tidal estuary. Ocean Model 89:29-44
- 5) Guillaume, A., and Wells. J.C. "Gyre generation after a typhoon-induced upwelling in a stratified lake." International Symposium on Stratified Flows. Vol. 1. No. 1. 2016



# Safety Performance Analysis of Unsignalized Mid-block Crosswalks: An Agent-based Approach for Pedestrian-vehicle Interactions

Kalambay Ilunga Panick

Transportation and Spatial Planning Laboratory, Department of Civil Engineering

**Key Words:** Agent-based approach, Mid-block crosswalk, Pedestrian-vehicle interaction, degree of courtesy

## 1. Introduction

Road infrastructure is strongly linked to fatal and serious injury causation in road traffic collisions. The number of road traffic deaths in the world continue to climb, reaching a substantially high of 1.35 million in 2016. Pedestrian safety has become a priority for many cities all over the world since road accidents continue to be a health and social problem for both high-income and less developed countries. Furthermore, today 55% of the world's population lives in urban areas, a proportion that is expected to increase to 68% by 2050.

Hence, there is a huge need to create a crash-free society where all road users can perceive pedestrian facilities as much safe as possible. This means minimal threat or conflict with motor vehicles especially at unsignalized crosswalks where pedestrians are expected to cross anytime.

This study aims to contribute to ensuring safer roads by building through microsimulation a model of pedestrian-vehicle interactions at unsignalized mid-block crosswalks based on drivers' courtesy.

The unsignalized mid-block crosswalk between Handai-byoin Mae station and Osaka University Hospital has been chosen as the case study thanks to the power of Osaka University Hospital. That crosswalk is particularly interesting because of its mixed traffic that might be difficult to find anywhere in Japan. It is used by a wide range of road traffic users from the elderly who visit the hospital to Osaka University students. Also, in Japan authorizations have to be granted to conduct a video survey to collect any data in the road environment. There are compulsorily required, and permission may fail due to privacy reasons.

## 2. Methodology

The figure below shows the location of the unsignalized mid-block crosswalk.



Fig. 1 Location of the unsignalized mid-block crosswalk.

A questionnaire survey, a video survey and the simulation of interactions between vehicles and pedestrians have been carried out in this study.

### 2.1 Data collection

A questionnaire survey has been conducted to grasp the transportation modes used by people who visit the hospital or the university and the usability of the crosswalk.

The observation time for the video survey has been divided into 10-minute intervals corresponding to the arrival of trains at the monorail station.

The targeted pedestrian crossing is a one-stage crosswalk with continental marking patterns on a two-way roadway. The road is located in an urban street environment with a speed limit of 30 km/h. Widths of and the crosswalk and vehicle lanes are respectively 10 m and 3.6 m. The length of crosswalk markings and the spacing between adjacent crosswalk markings are both 0.45 m.

The video camera recording with manual data extraction was performed on December 3<sup>rd</sup>, 2018 from 8h00 a.m. to 9h00 using the software Tracker 5.0, a video analysis and modeling tool. Pedestrian speeds, vehicle speeds and Post-Encroachment Times (PET) have been extracted. 209 crossing episodes have been selected and pedestrians were tracked while crossing the road freely without any interaction with motor vehicles. 66 driving episodes of vehicles in free-flow speeds were also tracked. 53 episodes for PET extraction have been chosen.

### 2.2 Model development, calibration, and validation

Most of the simulation platforms such as VISSIM, PARAMICS are designed for normal and safe traffic operations t (travel time, delay, etc.) rather than traffic interactions or surrogate safety assessment. Therefore, when used in traffic safety studies they pose problems. We have developed an agent-based approach using NetLogo, a generic simulation software. Since its environment was not designed with any specific domain of application in mind, the modeling of non-ideal real-world scenarios could be widely explored.

Three sets of assumptions have been considered to reproduce as much as possible several characteristics of real-world traffic flow.

*Assumption 1.* Each driver has his/her own maximum speed and decides whether to yield for pedestrians at the crosswalk or not according to his/her own degree of courtesy.

*Assumption 2.* Each pedestrian has his/her own walking/crossing speed and his/her walk time before willing to cross the road

*Assumption 3.* Once at the crossing point, pedestrians communicate their desire to cross to drivers.

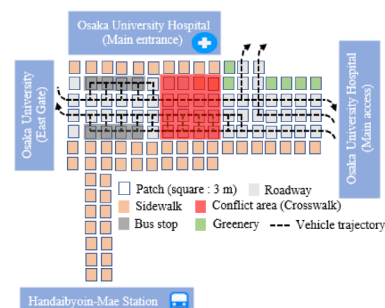


Fig. 2 Reproduction of the unsignalized midblock intersection.

The crosswalk has been divided into four parts as shown in the



figure below.

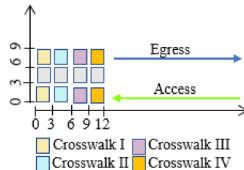


Fig. 3 Description of the crosswalk layout.

### 3. Results

#### 3.1 Questionnaire survey and video survey

As a result of the questionnaire survey, among the 3337 respondents, 37% use public transportation means (train, monorail, bus), 35.8% use non-public transportation means, 2.2% prefer walking while 24.3% counts for other means and no answers. They would like to cross the road with ease. Respondents over 65 years old represent a share of 43.1%.

The variability of pedestrian flows and vehicle traffic volumes have been highlighted. Results have shown an average of 209 vehicles for the bidirectional pedestrian flow, singly 204 and 5 from the station side and hospital side and an average of 66 vehicles for the bidirectional flow (53 and 13 in access and egress lanes).

209 crossing episodes have been selected and pedestrians were tracked while crossing the road freely without any interaction with motor vehicles. 66 driving episodes of vehicles in free-flow speeds were also tracked. 53 episodes for PET extraction have been chosen. Here PET is defined as the time between a pedestrian leaving a common spatial zone and the vehicle arriving in that zone. The results of the video tracking analysis have shown that pedestrian with normal speed (1.4 m/s) counted for 17% of the total number. About 10% walked below 1.1 m/s. The mean speed has been evaluated at  $1.53 \pm 0.28$  m/s. 90% of drivers drove up to 30 km/h. The minimum and maximum recorded vehicle speeds were 12.46 km/h and 37.8 km/h. More than 80% of drivers were not yielding for pedestrians before the stop line. Most of the PET values were between 0.42 s and 1.42 s.

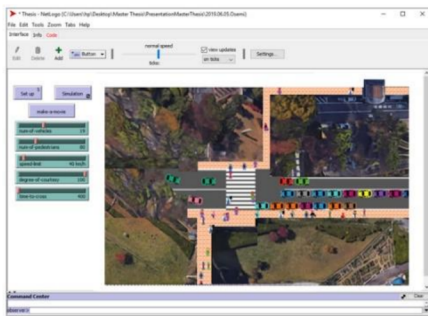


Fig. 4 Model interface.

Theil's inequality coefficient  $U$  has been used as the goodness of-fit measure for validating the model ( $U \leq 0.2$ ). Pedestrian speeds, vehicle speeds, and PET have been simulated for different selected episodes. Theil's inequality coefficients of the three parameters for the access side were individually 0.013, 0.026 and 0.15.

#### 3.2 Simulation of pedestrian-vehicle collisions

Since the yielding compliance varies from a driver to another, we have simulated pedestrian-vehicle collisions based on the degree of courtesy randomly distributed among drivers. The highest degree of courtesy is 100 and the lowest is 0. That expresses the probability of yielding for pedestrians.

Vehicles speeds and pedestrian speeds have been randomly respectively distributed between 10 and 40 km/s and 0.6 and 2 m/s.

2019 collisions have been recorded. Table 1 shows the number of collisions recorded for five ranges of degrees of courtesy. Ten runs have been carried out for each range of degree of courtesy.

Table 1 Number of collisions.

Degree of courtesy	Number of collisions
0-20	1242
21-40	581
41-60	135
61-80	51
81-100	10

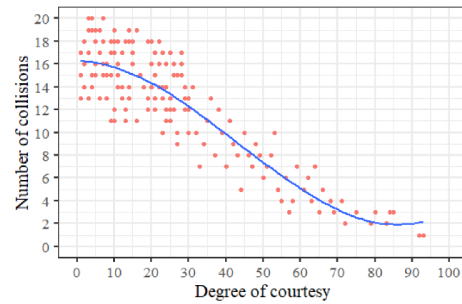


Fig. 5 Variability of number of collisions.

Figure 6 shows the pedestrian-vehicle collisions recorded on the access vehicle lane for 7 specific times.

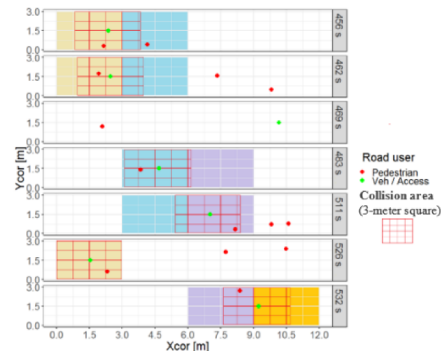


Fig. 6 Pedestrian-vehicle collision on the access vehicle lane.

### 4. Conclusions

A model of pedestrian-vehicle interactions has been proposed for unsignalized mid-block crosswalks based on drivers' degrees of courtesy. Interactions between pedestrians and vehicles have been simulated to grasp the variability of the number of collisions while degrees of courtesy have been randomly distributed among drivers. It has been shown that the number of collisions mainly depends on drivers' courtesy. The higher the degree of courtesy, the fewer pedestrians are subject to a collision. The likelihood of collisions is linked to the lack of priority compliance towards pedestrians. Education of road users, especially drivers is prominent to make roads safer.

Also, safety improvement measures such as the installation of speed humps can enhance drivers' courtesy to give the right-of-way to pedestrians.

Even though pedestrian-vehicle collisions have been simulated, in real life, humans' decision-making and action process are far more complex than our current model simply based on the degree of courtesy. Different aspects of this parameter can be improved in the future by conducting behavior studies in a more detailed microscopic level.

# Full Scale resistance Prediction of paint surface

## Proposal of new approximate formula for friction with roughness

Ren Xu

Hull Form Design Sub-Area, Department of Naval Architecture and Ocean Engineering

**Key Words:** Frictional resistance, surface roughness

### 1. Introduction

Both the environmental pollution problem and high fuel costs demands ship and shipping industry to find a way for saving energy. Reduction of hull resistance is one of the ways to improve energy efficiency. As frictional resistance account for a major part in ship total resistance, especially for low speed large block coefficient ship, reducing the frictional resistance of ships is a very significant way for energy saving. So many new low friction coating have been proposed and have been used for the real new ships and existing ships to reduce the fuel consumption. But the testing methods of new coatings and prediction method based on experimental results have not been fully established. Inoue et. al. made the experiments using 3m and 5m simple models with different coatings and determined the equivalent sand roughness based on the measurement results. They predicted the full scale frictional resistance based on estimated equivalent sand roughness. On the contrary, Kawashima et. al. did the resistance test for 2m flat plate model with two (long and short) wave length surface roughness plate and 14m plate with medium wave length roughness. They showed the resistance coefficient increase by medium flat plate does not show the intermediate value between two 2m plate long model with long and short roughness. They also show the mean shear stress of plate for each speed vs resistance coefficient increase and they could explain the roughness effect. They predicted 200m ship resistance increase by their proposed method.

In the first stage of this research, the equivalent sand roughness hypothesis is tested using Kawashima et. al. data. The results show the promising results.

So, in the second stage, new approximate formula of frictional resistance is proposed based on the computed results by the extended method of Katsui for roughness surface. The equation is function of two Reynolds number based on plate length and equivalent sand roughness height.

### 2. Calculation

In this study, the frictional resistance coefficient is calculated by logarithmic law with Coles law of the wake following Katsui and White function of surface roughness:

$$\frac{u}{u^*} = \frac{1}{\kappa} \ln\left(\frac{u^* y}{\nu}\right) + 5.0 - \Delta B + \frac{\Pi}{\kappa} \left\{ 1 - \cos\left(\pi \frac{y^+}{\delta^+}\right) \right\} \quad (1)$$

$$\Pi = 0.62 - 1.21 \exp\left(-\frac{\delta^+}{290}\right)$$

$$\Delta B = \frac{1}{\kappa} \ln(1.0 + 0.3k^+)$$

Substitute function (1) into the definition of momentum thickness

$$\begin{aligned} \theta &= \int_0^\delta \frac{u}{U} \left(1 - \frac{u}{U}\right) dy \\ &= \delta \left[ \frac{\zeta}{\kappa} (1 + \Pi) - \left(\frac{\zeta}{\kappa}\right)^2 \left\{ 2 + 2\Pi(1 - A) + \frac{3}{2}\Pi^2 \right\} \right] \\ \zeta &\equiv \frac{u^*}{U}, \eta \equiv \frac{y}{\delta} \end{aligned} \quad (2)$$

The momentum thickness can be solved by momentum integral equation as below:

$$\frac{d\theta}{dx} = \zeta^2 = \frac{1}{2} C_f \quad (3)$$

From equation (2) and (3), we could calculate the frictional resistance coefficient with different surface roughness.

### 3. Comparison with Experiments

Inoue et.al have tested previous calculation with the experiment results by Osaka University<sup>1)</sup> which shows that we could determine the equivalent sand roughness by previous method. In this study, we made a new program similar as Inoue and tested this program with the experiment data from NMRI.

National Maritime Research Institute have done flat plate experiment with different surface roughness. The flat plate experiment using 2m flat plate with short and long wavelength roughness surface, and 14m flat plate with medium wavelength roughness surface. The original data sets were provided by NMRI

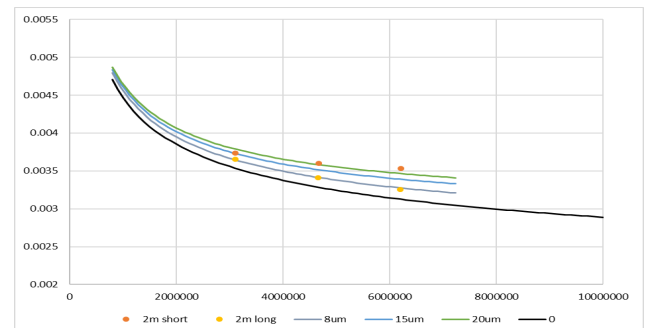


Fig.1 Comparison of experiment results by NMRI of 2m flat plate and computational calculations.

Fig.1 shows that the calculations of the 8μm and 20μm agree with the experiment results of long and short wavelength roughness. So we considered the equivalent sand roughness of medium wavelength roughness should be about 15μm in the middle of 8μm and 20μm.

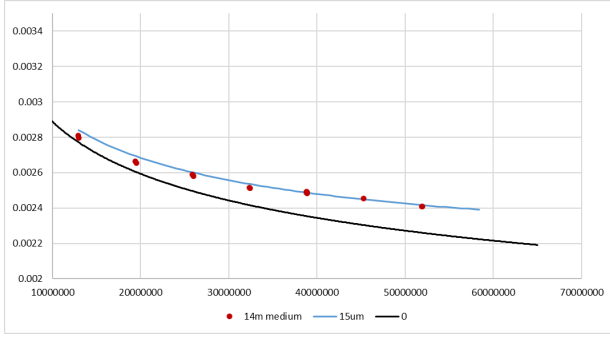


Fig.2 Comparison of experiment results by NMRI of 14m flat plate and computational calculations.

Fig.2 shows that the calculation of 15 $\mu$ m agree with the experiment results of medium wavelength roughness. It means the estimation given by 2m model is reasonable.

As the comparison between calculation and experiment data shows good agreement for very heigh  $Rn$ , we could predict the coating resistance of 14m model based on the 2m model experiments. So, it suggest that the prediction of full scale can be done using equivalent sand roughness concept.

#### 4. Approximate Formula

The previous calculation of frictional coefficient is complex which is not easy to be widely used. In this chapter, we propose an approximate formula which could be easily calculated.

Katsui's formula<sup>3)</sup> shows good agreement with Osaka's new experiment and could calculate frictional resistance coefficient for smooth surface, the calculation data of Prof. Katsui's formula is expressed as  $C_{F0}$

$$C_{F0} = \frac{0.0066577}{(\log Rn - 4.3762)^{0.042612 \log Rn + 0.56725}} \quad (4)$$

For the trend line by binomial expression between  $\log_{10} Rn$  and  $C_F(Uk/\nu) * \log_{10}^2 Rn / C_{F0}$  shows good correlation, we propose the approximate function as below:

$$C_F\left(\frac{Uk}{\nu}\right) = C_{F0} \left( A_0 - \frac{A_1}{\log Rn} + \frac{A_2}{\log^2 Rn} \right) \quad (5)$$

$A_0, A_1, A_2$  are parameters calculated from roughness Reynolds number  $Uk/\nu = \text{constant}$  (0~2000).

We calculated frictional resistance coefficient of different equivalent sand roughness (15 $\mu$ m, 55 $\mu$ m, 85 $\mu$ m) with same ship speed by the approximate function shows in Fig.3.

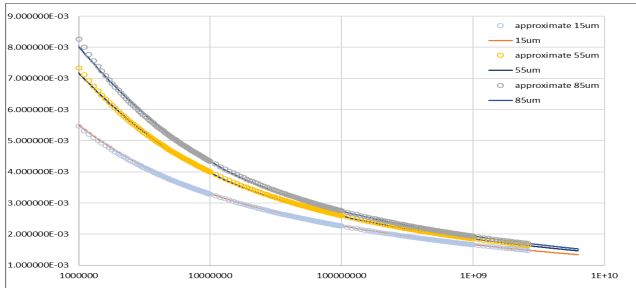


Fig.3 Comparison of calculations by program and approximate function with same ship speed.

Fig.3 shows that the estimated frictional coefficient of 15 $\mu$ m, 55 $\mu$ m and 85 $\mu$ m could also fit the computation line with good accuracy although frictional resistance for those roughness are not used to redict the simple approximate formula.

We also calculated the frictional resistance coefficient with different ship speed shows as Fig.4

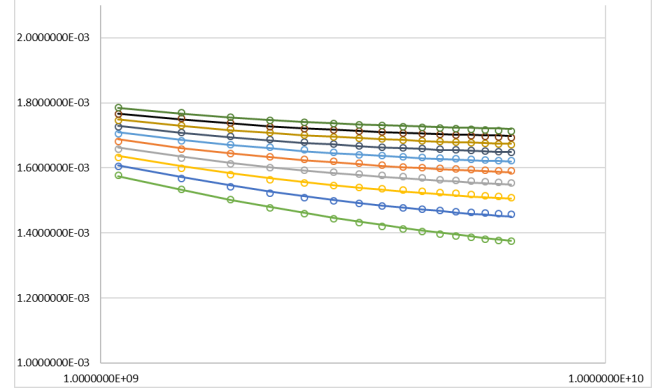


Fig.4 Comparison of calculations by program and approximate formula with different ship speed.

In Fig.4, lines are the computational results and circles are calculation results by approximate function which also shows good correlation.

#### 5. Conclusions

In this study, we calculated frictional resistance coefficient by logarithmic law with Coles law of the wake and White function of surface roughness, and the comparison with the experiment data of National Maritime Research Institute shows promising results to support the equivalent sand roughness concept. The measurement of surface roughness is difficult and same geometrical roughness with different materials shows the different frictional resistance performance. So, by comparing the experiment data with the calculation lines, the equivalent sand roughness of painting surface is estimated and full scale performance with the tested coating can be predicted by simple formula. The previous approximate formula proposed by Inoue et. al. was not accurate, So, in this study, the approximate formula by the parameter from roughness Reynolds number  $Uk/\nu = \text{constant}$  is proposed. By comparing the estimated result with the program computation shows good agreement for the  $Rn = 1.0 \times 10^6 \sim 1.0 \times 10^{10}$ , the proximate function could be used for calculation of the frictional resistance coefficient for full scale ship.

The author express her gratitude to Dr. Hideki Kawashima and Dr. Hirihsa Mieno for providing the data of the collaborative research between National Maritime Research Institute, Japan and Chugoku Marine Paints, Ltd, Japan.

#### References

- 1) Inoue, R: A consideration on the resistance test of the model with paint roughness, JASNAOE Conference Proceedings 15, pp.77-80, 2012.
- 2) Kawashima, H: Scale effect on frictional resistance of painted rough surface-Comparison of frictional resistance of long and short painted rough surface flat plate, JASNAOE Conference Proceedings 24, pp.729-734, 2017.
- 3) Katsui, T: The proposal of a new friction line, Proceedings of the 5th Osaka Colloquium, pp.76-83, 2005.

# Study of Dolphin Swimming Performance by CFD

Yujia YAO

Marin Mechanism System Engineering, Department of Naval Architectural and Ocean Engineering

**Key Words:** Dolphin, CFD, Oscillation motion, Thrust

## 1. Introduction

Marine life has excellent swimming performance because of nature selection. Among various species, dolphin has high speed and high efficiency when swimming and has been an area of interest for both biologists and engineers to develop an energy efficient propulsion mechanism for applications on a variety of vehicles ranging from underwater robots as well as surface cruising robots to ultimately, ocean-going ships.

Gray (1936) pointed out that the propulsion performance of a dolphin is seven times larger than that of any land mammal. He obtained this conclusion based on the assumptions that the maximum speed of dolphins is 20 knots (10 m/s), the friction drag of the dolphin body can be estimated by assuming the boundary layer around the body is turbulent and the propulsive efficiency is 100%. In the same paper, he also pointed out that if the propulsion performance of dolphins is similar to terrestrial mammals, these very high swimming speeds are due to the laminar boundary layer around the dolphin body. However, after an extensive study, Fish (1993) concluded that the dolphin swimming speeds are not related to the boundary layer around the dolphin.

Therefore, it is necessary to understand the effect of dolphin swimming pattern on its very high propulsive performance. Isogai (2014) carried out numerical analysis on the flow around the caudal fin of a bottlenose dolphin (*Tursiops truncatus*) by a 3D Navier-Stokes (NS) approach. In his work, computations were conducted based on the standing swimming motion of dolphin, neglecting the effect of flow around the dolphin body as well as the interaction between the body and caudal fin. However, it is necessary to include these effects in order to fully understand the dolphin swimming mechanism.

The numerical simulation of dolphin swimming pattern developed by Xiaozhou Wang (2018) is inconsistent with the real situation. The thrust should be higher when using swimming pattern which is close to real dolphin motion. Thus, in this paper, the simulation of swimming pattern which is similar to real situation has been developed and compared with the mode of Xiaozhou Wang. The thrust of each pattern is calculated and we can see the pattern which is similar to real dolphin swimming motion can generate larger thrust. And in the future research, real dolphin swimming data should be obtained to get reliable swimming pattern.

## 2. Methodology

### 2.1 Numerical Method

In this research, numerical analyses were carried out to understand the flow around the body of a swimming dolphin by solving 3D Reynolds Averaged Navier-Stokes (RANS) Equations in an open-source finite volume framework, OpenFOAM. In order to compute an unsteady flow around a moving body (the

dolphin), a single phase transient flow solver was used with moving mesh techniques. The Reynolds Averaged Navier-Stokes (RANS) Equations can be written as below:

$$\int_V \frac{\partial \rho \phi}{\partial t} dV + \int_V \nabla \cdot (\rho u \phi) dV - \int_V \nabla \cdot (\rho \Gamma_\phi \nabla \phi) dV = \int_V S_\phi dV$$

### 2.2 Assumption and Turbulence Model

Since the purpose of this step is to estimate the flow behavior around a dolphin, the dolphin is assumed to be in a fresh water at room temperature rather than in cold sea water. Therefore, the kinematic viscosity and density of fluid were assumed to be that of fresh water. The effect of free-surface on the flow field as well as the dolphin body was neglected. Moreover, the fluid is fresh water which is incompressible and no cavitation occurred during the dolphin motions. Thus, an incompressible transient single-phase flow solver was used. The effects of dolphin skin on the boundary layer such as skin roughness are neglected in this analysis. The dolphin skin is assumed to be a smooth, water-tight body without nostrils. The dolphin is in neutral buoyancy with no significant gravitational, buoyant and Coriolis forces affecting its motion as well as the flow field. The inflow is a uniform flow with medium turbulence intensity (5%). The body of the dolphin is an isotropic material without any form of nonlinearities including geometric and material non-linearities. The motion of the body surface is directly proportional to that of the backbone.

Based on these assumptions, the Reynolds number for this scenario is estimated to be approximately  $1.5 \times 10^7$ . Therefore, it is necessary to carry out turbulence modelling in the computations. Spalart-Allmaras turbulence model was chosen due to its stability and the lack of severe flow separation due to streamline shape of the dolphin.

## 3. Simulation

### 3.1 Definition of Fin/Body motion

The motion algorithm for general fish swimming was developed based on the mathematical model proposed in Wolfgang et al. (1999) with the assumption that the displacements of the body-surface is the same as that of the backbone of fish. According to their observations, the time-dependent transverse motion of a fish in two dimensional reference frame can be expressed as:

$$z(x, t) = A_l a(x) \sin(\omega t - kx)$$

where  $k$  is wave number of body motion,  $\omega$  is the period of body motion,  $A_l$  is amplitude of the deformation expressed in the ratio of body length  $l$ . And  $a(x)$  describes the shape of backbone deformation which can be expressed by a sixth-order polynomial function as below:

$$a(x) = Ax^6 + Bx^5 + Cx^4 + Dx^3 + Ex^2 + Fx + G$$

Where A, B, C, D, E, F, G are coefficients.

Fig.1 shows the pressure field on the dolphin body, Fig.2



shows the grid around the dolphin body. Fig.3 shows the velocity field around the flapping dolphin.

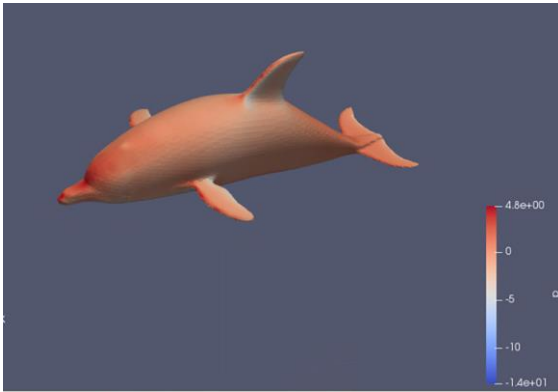


Fig. 1 Pressure field on the dolphin body

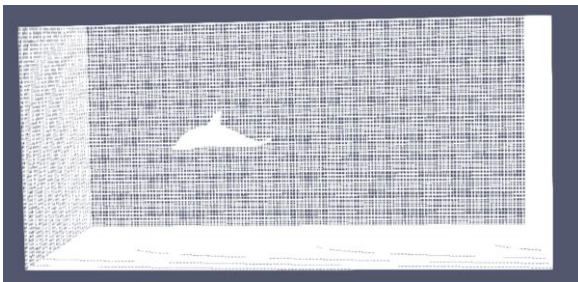


Fig. 2 Grid around the dolphin body

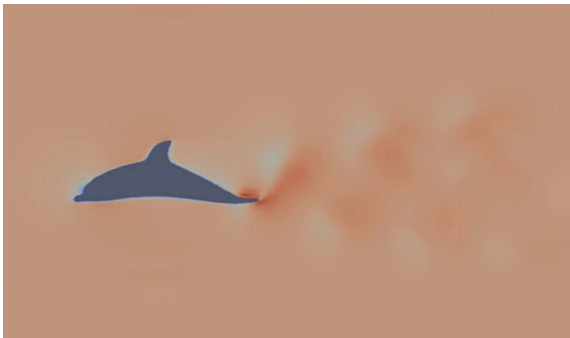


Fig.3 Velocity field around the flapping dolphin

### 3.2 Derivation of Hydrodynamic Force by CFD

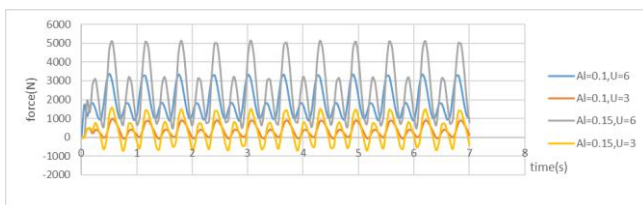


Fig. 4 The hydrodynamic force when frequency is equal to 2Hz

The hydrodynamic force is obtained by integrating pressure and shear stress around the dolphin body. The hydrodynamic force when frequency is equal to 2Hz is shown in Fig.4. Because the dolphin conducts oscillation motion, the hydrodynamic force is also periodic. Two amplitudes of peak-to-peak tail motion are chosen for this study: 10%, 15%

length of the body which will be described as small and middle amplitudes. Table 1 shows the derived thrust of small amplitude fluke motion. Table 2 shows the thrust comparison obtained from this research and in Xiaohou Wang's research.

Table 1 Thrust derived under small amplitude fluke motion

	U (m/s)	Thrust (N)
f=1Hz	1	45.366
	3	-109.306
f=2Hz	1	172.227
	3	9.396
f=3Hz	1	854.062
	3	416.217

Table 2 Thrust (N) compared with WANG's result

	Wang(2018)	Present
f=1Hz	10.5878	45.366
f=2Hz	34.6834	172.227
f=3Hz	84.1642	854.0616

### 4. Conclusions

From the CFD simulation, the hydrodynamic force of swimming dolphin is obtained. Compared to Xiaozhou Wang, the motion equation used in this paper obtained larger thrust of swimming dolphin, this shows that the large thrust of real dolphin swimming is related to the swimming pattern.

And we can see the thrust increases as amplitude increases and also increases as the frequency increases.

In future research, the geometry model obtained from real dolphin should be used and dolphin swimming motion of large amplitude and high velocity should be conducted to get reliable thrust.

### References

- 1) Fish, F. E.: Power output and propulsive efficiency of swimming bottlenose dolphins (*tursiops truncatus*). Journal of Experimental Biology, pp.179–193,1993.
- 2) Gray, J.: Study in animal locomotion iv-the propulsive powers of the dolphin. J. Exp. Biol., pp.192–199,1936.
- 3) Isogai, K.: Effect of flexibility of the caudal fin on the propulsive performance of dolphins,2014.
- 4) Ltd, O.: Openfoam v1706: New and improved numerics, 2017.
- 5) Wolfgang, M., Anderson, J., Grosenbaugh, M., Yue, D., and Triantafyllou, M.: Near-body flow dynamics in swimming fish. Journal of Experimental Biology, pp.2303–2327.38,1999.
- 6) Xiaozhou Wang, Peng Wei, Ye Yuan, Zhiguo Zhang, Dakui Feng.: Evaluation of Dolphin Swimming Speed and Thrust Based on CFD, ISOPE Journal Paper, Vol.28, No.2, pp.120-127,2018.

# Study on Measurement Method of Under-Film Corrosion's Incubation Life Using Fe (II) Fluorescent Indicator

Azhan Bin Abdul Halim

Ocean Material Engineering Laboratory

Department of Naval Architecture and Ocean Engineering

**Key Words:** Nondestructive monitoring, under-film corrosion, water ballast tank, Fe (II), fluorescent indicator, spectrum imaging

## 1. Introduction

It is necessary to carry out nondestructive monitoring of under-film corrosion of anti-corrosion coated steel panels such as water ballast tanks (WBT) and investigate the statistical nature of the corrosion's incubation life to improve the structural safety of aging vessels. Hirayama et al.<sup>1)</sup> synthesized the compound (1S)-3'-(diethylamino)-N,N-diethyl-3-oxo-3',9a'-dihydro-3H-spiro[isobenzofuran-1,9'-xanthen]-6'-amine-oxide or RhoNox-1 that reacts with Fe (II) to produce chelation-enhanced fluorescence (CHEF). Osawa et al.<sup>2)</sup> prepared semi-transparent epoxy paint added with RhoNox-1, conducted corrosion tests for several steel panels coated with it and confirmed the corrosion detection of RhoNox-1. Several scribed test panels were exposed to sodium chloride solution drops to introduce initial corrosion and then coated, were used in this study. Because of this, Fe (II) was formed before or after the start of corrosion test and it was not possible to determine the corrosion's incubation life.

The purpose of this study is to develop a method to measure the corrosion's incubation life by detecting the forming of Fe (II) under the coating film. The anti-corrosion coating system for actual WBTs has high corrosion resistance and it takes years to generate detectable amount of Fe (II). In this study, it is necessary to compare corrosion's incubation lives by changing the steel type, coating specification as well as corrosion environment. For this purpose, it is important to shorten the test time by using coated test panels whose corrosion resistance has been lowered to an extent that Fe (II) formation could be detected in a short time. The anti-corrosion performance of the paint can be controlled by mixing multiple hardeners with different anti-corrosion performances.

In this report, several hardeners were mixed and semi-transparent epoxy paints containing RhoNox-1 with different anti-corrosion performance were prepared. Corrosion tests of the steel panels coated with the RhoNox-1-containing paints were conducted. During the corrosion tests, spectrum imaging (SI) measurements of the coating surface were performed to detect Fe (II) formation on the surface under the coating film without initial corrosion.

## 2. Coating specification

A side of rectangular panels of high tensile strength steel for shipbuilding, with dimensions 150mm×35mm×3.2mm, blast grade Sa 2.5, surface roughness Rz 30μm, were coated with a clear two-pack epoxy paint; main agent and hardener. The hardener for the epoxy paint was prepared by mixing a PSPC-certified hardener for WBT paints; Hardener H with high corrosion resistance and Hardener L with low corrosion resistance, to adjust the anti-corrosion performance to be significantly reduced compared to the actual paint. Each test plate was coated with the paint with designated target dry film thickness (DFT).

Table 1 Hardener mix ratio and target DFT for test panels.

Test plate	H:L	Target DFT (μm)
E41, J41	50:50	50
E58, J58	100:0	50
E62, J62	100:0	100
E66, J66	100:0	200

## 3. Fluorescence measurement and test condition

RhoNox-1 was synthesized in an amount sufficient to coat the test panels with the same material and synthesis method as previous report<sup>2)</sup>. RhoNox-1 does not produce prematurely fluorescent CHEF by the reaction with amine, which is the main component of the epoxy paint's hardener, but emits fluorescence at around 570 nm when reacting with Fe (II).

Due to the limitations of the equipment used for this study, the confocal laser scanning microscopy (CLSM) measurement was performed at  $\lambda_{ex}=473$  nm. It was observed that the reaction between RhoNox-1 and Fe (II) can be detected by the increase in emission intensity around  $\lambda_{em}=570$  nm<sup>2)</sup>. The test panels were subjected to immersion test with water at 50 °C and the fluorescence measurement of the coated surface of test panels was conducted.

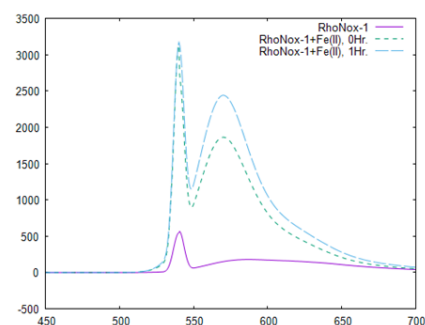


Fig. 1 Fluorescence spectrum of RhoNox-1 with or without FSA(II) in DMSO ( $\lambda_{ex}/\lambda_{em}=540$ nm/570nm).



Fig. 2 RhoNox-1-coated panels subjected to immersion test.

#### 4. SI measurement

The fluorescence measurement was performed according to the following procedure. A rectangular measurement area for SI of 2.5 mm side lengths or 800×800 pixels was set at two locations on each test panel. The SI measurement area was divided into rectangular areas with dimensions of 10×10 pixels (hereinafter referred as “area elements”).  $\lambda$  mode measurement was performed to acquire SI data of the whole measurement area, light emission intensity was averaged within each surface element, and the averaged spectrum of each surface element was calculated. The averaged spectrum was subjected to Savitzky-Golay smoothing of order  $k=2$  and half band width  $n=3$ , and the maximum wavelength  $\lambda_{\max}$  and the maximum emission intensity  $I_{\max}$  of each element were calculated.

As shown in Figure 1, RhoNox-1 used in this study emits maximum fluorescence intensity around  $\lambda_{\text{em}}=570$  nm when it reacts with Fe (II). Therefore, if Fe (II) is formed under the coating during immersion test, it is expected that  $I_{\max}$  will increase and  $\lambda_{\max}$  near 570 nm at the anode part.

#### 5. Fluorescence emission characteristics

Figure 3 shows the box plot of each surface element  $I_{\max}$  for several panels. The thick lines in the box plot represent the median  $Q_{2/4}$ , the upper and lower sides of the box represent the third quartile point  $Q_{3/4}$  and the first quartile point  $Q_{1/4}$ , and the upper and lower whiskers represent the upper and lower limits of the section of the following equation.

$$[Q_{1/4} - 1.5IQR, Q_{3/4} + 1.5IQR]; \quad IQR = Q_{3/4} - Q_{1/4} \quad (1)$$

The  $I_{\max}$  contours for two panels, E58 and J58 are shown in Figure 4 with the colour level of the contour. The test panels here were conventional steel and corrosion-resistant steel respectively coated with the paint that have the same corrosion resistance.

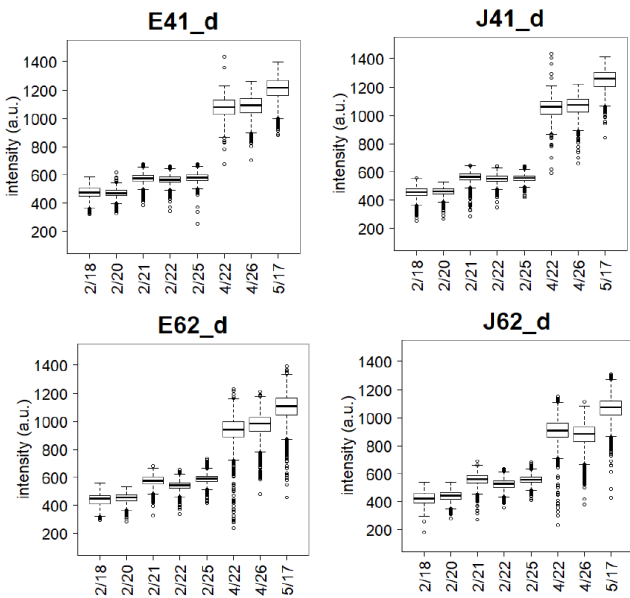


Fig. 3 Comparison of  $I_{\max}$ 's boxplots of different panels.

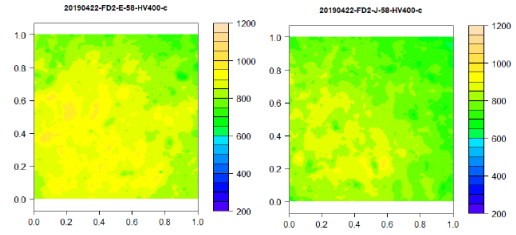


Fig. 4 Comparison of  $I_{\max}$ 's contour maps of panels E58 and J58 during the hot water immersion test.

#### 6. Conclusions

Several hardeners were mixed to prepare RhoNox-1-containing semi-transparent epoxy paint with different anti-corrosion performances. Corrosion tests for the steel panels coated with the prepared RhoNox-1-containing paint were conducted. During the corrosion tests, spectrum imaging (SI) of the coated surface was performed to detect Fe (II) formation on the surface under the coating film without initial corrosion. The findings obtained in this study can be summarized as follows.

(1) Coated test panels using the RhoNox-1-containing semi-transparent paint prepared in this study were prepared. By evaluating the fluorescence maximum wavelength and maximum emission intensity for each rectangular area of 10 pixels side length from SI result, it is possible to estimate the spatial distribution of Fe (II) formation and increase due to the under-film corrosion. This indicates that it is possible to measure the under-film corrosion's incubation life and the degree of anodic reaction progress under the coating film by fluorescence measurement using the RhoNox-1-containing semi-transparent paint developed in this study.

(2) Under the test conditions in this study, it was shown that as for test panel with the higher mixing ratio of high corrosion resistance hardener and dry film thickness, the formation of Fe (II) was slower and the progress of corrosion was slower. This result indicates that the fluorescence measurement using RhoNox-1-containing semi-transparent paint developed in this research may be able to evaluate the effect of the factors such as coating specification and steel type influencing the under-film corrosion's incubation life.

#### References

- 1) Hirayama, T., Okuda, K., Nagasawa, H. (2013) "A Highly Selective Turn-on Fluorescent Probe for Iron(II) to Visualize Labile Iron in Living Cells," Journal of Royal Society of Chemistry, 4, pp. 1250-1256.
- 2) N. Osawa, A. Takada, T. Kojima, S. Takano (2015) "Development of Fe(II) Fluorescent Indicator for Under-Film Corrosion Monitoring of Epoxy-coated Steel Panels," Proceedings of The Japan Society of Naval Architects and Ocean Engineers, 21, pp. 93-99.